

Divergent convective outflow in ICON deep convection-permitting and parameterised deep convection simulations

Edward Groot^{1,2}, Patrick Kuntze¹, Annette Miltenberger¹, and Holger Tost¹

¹Institut für Physik der Atmosphäre, Johannes Gutenberg Universität, Johannes-Joachim-Becher-Weg 21, Mainz, Germany

²Atmospheric, Oceanic and Planetary Physics, University of Oxford, Sherrington Road, Oxford, UK

Correspondence: Edward Groot (egroot@uni-mainz.de)

Abstract. Upper-tropospheric deep convective outflows during an event on 10th-11th of June 2019 over Central Europe are analysed ~~from simulation output in ensembles~~ of the operational numerical weather prediction model ICON. Both ~~a~~ parameterised and an explicit representation of deep convective systems are studied. Near-linear response of deep convective outflow strength to net latent heating is found for parameterised convection, while ~~coherent patterns in variability are a~~ different but physically coherent patterns of outflow variability is found in convection-permitting simulations at 1 km horizontal grid spacing. ~~Furthermore, three hypotheses on factors that may affect the magnitude of the convective outflow are tested in the convection-permitting configuration: organisation of convection through dimensionality of the systems, organisation of convection through aggregation and convective momentum transport. We investigate if the conceptual model for outflow strength proposed in our previous idealised LES-study is able to explain the variation in outflow strength in real-case scenario.~~

5

10 Convective organisation and aggregation induce a non-linear increase in the magnitude of deep convective outflows with increasing net latent heating ~~, as shown by the confidence interval of the best fit between power transformed net latent heating and detected magnitude of outflows. However, mixed and weaker than expected signals are found in an attempt to detect the representation of dimensionality of the convection and its consequences for the divergent outflows with an ellipse fitting algorithm that describes the elongation of the intense (convective) precipitation systems. As opposed to expectations,~~

15 ~~convective momentum transport is identified to slightly increase the magnitude of divergent outflows in this case study in convection-permitting simulations, consistent with the conceptual model. However, in contrast to expectations from the conceptual model, a dependence of the outflow strength on the dimensionality of convective overturning (2D versus 3D) cannot be fully corroborated from the real-case simulations.~~

20 Our results strongly suggest that the interactions between gravity waves emitted by heating in individual deep convective elements within larger organised convective systems are of prime importance for the representation of divergent outflow strength from organised convection in numerical models.

1 Introduction

~~Flow variability may be defined as the evolution of differences in the horizontal winds originating from initial condition uncertainty in a model ensemble. However, it may also be defined as the analysis of a specific flow characteristic of a~~

25 ~~distribution with respect to its median or mean. Lorenz derived expressions for difference evolution of a flow (Lorenz, 1969) in his fundamental research on predictability of atmospheric dynamics. He also demonstrated growth characteristics of initial condition derived flow variability towards the climatological distribution (i.e. the second possible definition)~~

It is well known that the process of (deep) convective organisation and clustering is an important actor in physics and dynamics of the Earth's atmosphere (e.g. Houze, 2004, 2018; Schumacher et al., 2004). Local heating by clusters of convective clouds can drive a flow that diverges away from the convective heat source in the upper troposphere. The divergent upper-tropospheric flow is accompanied by convergence at low levels. In recent work, Groot and Tost (2023b) have shown that on the one hand geometry and on the other hand clustering, organisation and aggregation of clouds within a convective system strongly affect the intensity of the induced divergent flow in the upper troposphere (when expressed per equivalent unit heating in a column). Idealised Large eddy simulations (LES) show that the amount of divergence differs between infinitely long squall lines and for instance regular multicells at fixed latent heating rates. Differences in strength of mesoscale divergent winds at a fixed (area average) column integrated heating rate as shown in the results of Groot and Tost (2023b) can be explained by variability in storm morphology and convective aggregation and these findings can be synthesised in a conceptual model (Figure 1), which is introduced later in this introduction. In this ~~century, predictability, meaning flow variability from the initial condition perspective, and its representation in work,~~ we aim to identify if convection-permitting and convection parameterised simulations of a real-case scenario display patterns of variability of outflow divergence with storm morphology, convective clustering and aggregation that are consistent with the conceptual model.

Comparing different representations of deep convection (i.e., LES, convection-permitting simulations and deep convection parameterisations) is important as forecast products are increasingly based on high-resolution simulations, while global ensembles of weather and climate simulations are currently treating deep convection as a parameterised process (e.g. Bechtold et al., 2014; Ollinaho et al., 2014). Moreover, one could assume that convective aggregation and organisation is less thoroughly represented in convection-parameterised simulations than in convection-permitting simulations (Done et al., 2006; Keane et al., 2014; Satoh et al., 2019; Lawrence and Salzmann, 2019).

In this work, a state-of-the-art numerical weather prediction (NWP) ~~models have been further investigated (e.g. Zhang et al., 2007; Baumgardner et al., 2014)~~ model is analyzed, with a focus on two ensembles with different spatial resolution and therefore representation of convection that cover a single convective event. An extensive methodology will be presented to investigate if the conceptual understanding (Figure 1; Groot and Tost (2023b)) can explain the coupling between dynamics and latent heating in ICON. If successful, the methodology could be useful for applications in further cases and regions around the world. In the following the conceptual model that links storm morphology, convective clustering and convective aggregation to different outflow geometries (accompanied by relative differences in the upper tropospheric divergence) is explained, based on Groot and Tost (2023b). After the explanation, the relation of the associated processes of gravity waves and convective organisation is shortly reviewed.

~~Flow variability can manifest at many different scales in atmospheric dynamics: from the smallest dissipative scales to planetary Rossby waves. In this study flow variability of mesoscale convection is assessed with the ICON numerical weather prediction~~

60 model, which represents a state-of-the-art operational forecasting and research model (Zängl et al., 2015; Giorgetta et al., 2018). In particular, the structure of divergent outflow variability induced by deep convection is examined. The role of convective organisation Conceptual model

Divergent and convergent flows can be interpreted as results of gravity wave emissions at the location of convective heating (e.g. Pandya and Durran, 1996; Houze, 2004).

65 Work fundamental for the interpretation of the conceptual model has been done in the late 1980s and dependence on precipitation rate will be assessed, based on hypotheses formulated

- following a study of Large Eddy Simulations (Groot and Tost, 2023b),
- and consistent with previous idealised models (Bretherton and Smolarkiewicz, 1989; Nicholls et al., 1991; Mapes, 1993)

70 The understanding of convective outflows in Groot and Tost (2023b) builds mainly on Bretherton and Smolarkiewicz (1989) based on their linearised gravity wave adjustment model an idealised expression of outflow strength from deep convection was constructed (Nicholls et al., 1991). Therein, deep convection is approximated by a localised heating source. The outflow depends linearly on the net latent heating, if the geometry of the heating source is prescribed. But the slope of the dependency differs between line sources and point sources of heating. Mapes (1993) investigates the consequences of the 1990s (Bretherton and Smolarkiewicz

75 , with some further studies appearing recently (e.g. Bierdel et al., 2017, 2018; Adams-Selin, 2020a, b; Weyn and Durran, 2017). The basic concept is that a warming tendency, representing the latent heating by cumulonimbus clouds as a localised heat source, continuously creates temperature and pressure, hence density, perturbations. The thereby modified atmospheric states often do not return to a background state immediately, but are maintained for some time: the perturbed state persists because updrafts can last for hours in a well-organised convective system. The outflow pattern is maintained, until the convective heating source ceases. The role of fluctuations in the intensity of a convective system has recently been documented and explained in Adams-Selin (2020a, b).

A continuous stream of upward moving parcels in a convective system results in continuously generated perturbations, leading to gravity wave adjustment conceptually for convective organisation: gravity wave activity may facilitate convective aggregation, which was suggested to affect outflow dimensionality by Groot and Tost (2023b). Consequentially, outflows from real convective systems conceptually tend to organise into a mixture of idealised point (within the convective system and in the surrounding atmosphere. The upper branch of the flow following such an adjustment mechanism in the plane perpendicular to a quasi-2D convective system (e.g. a squall line) is the divergent outflow from deep convection, which has been investigated in Nicholls et al. (1991); Pandya and Durran (1996).

85 In (?) explicit expressions for the linear component of the gravity wave response to basic localised heating geometries are derived: "3D point" and idealised line (sources (Figure 1a) and "2D") sources. In contrast to the results of Mapes (1993) and Mapes and Houze (1995), who found a reduction of the ratio of mass divergence to net latent heating caused by a stratiform heating influence compared to purely convective heating profile, the LES simulations of Groot and Tost (2023b) do not exhibit such behaviour; probably because of an only very weak stratiform contribution to the precipitation systems. "line" sources (Figure 1b) of latent heating have different outflow intensities. Work by Pandya and Durran (1996) using a more advanced

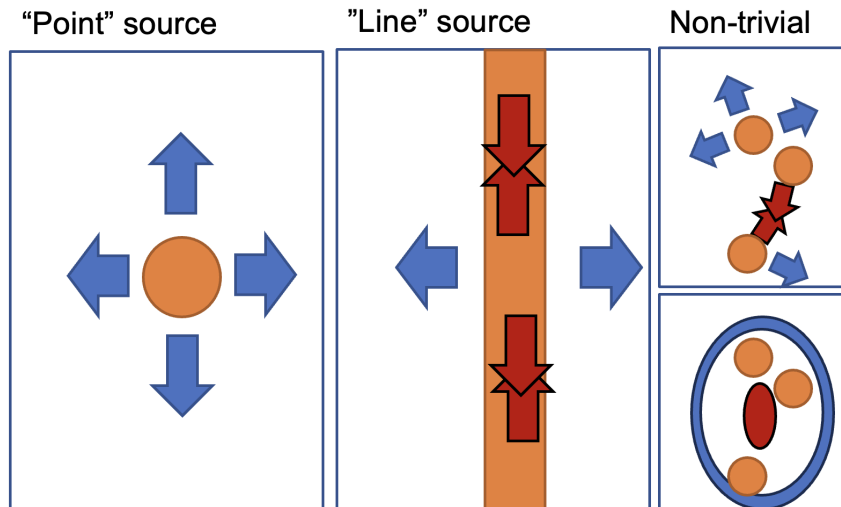


Figure 1. Top view of flow resulting from latent heating in convective updrafts (orange shading), as occurring in the upper troposphere. Left: a point source of heating with radially diverging flow. Center: line source of heating associated with squall lines leads to laterally diverging flow (blue arrows), but in the longitudinal direction, individual heating patterns along the squall line compensate: the diverging winds away from individual cells converge (red arrows) and neutralise divergent winds along the convective line. Right (top): complex situation with several updrafts in irregular positions relative to another, (bottom) which leads to a more complex pattern of divergence and convergence zones as outflows collide, simplified in the schematic with an oval orientation of those zones. Reality will be even more complicated. The conceptual understanding is based on Nicholls et al. (1991); Groot and Tost (2023b).

numerical simulation technique shows that the linear model by Nicholls et al. (1991) contains the dominant contributions to the resulting flow (linear approximation) and that the omitted non-linear terms are comparatively less important. Furthermore, Pandya and Durran (1996) argue based on the superposition principle that if a prototype heating pattern is inserted in a model of the atmosphere, the model contains a flow response closely resembling the flow expected from the linear model. Conceptually, this implies that local heat sources associated with updrafts behave as sketched in Figure 1.

From the perspective of Pandya and Durran (1996) any geometric pattern of heating can be seen as a superposition of a pattern of point sources (Figure 1). The most important notion is that radial divergence away from a small updraft ("point source") leads to more divergence at a given latent heating rate than lateral divergence, as associated with idealised line sources (and therefore very elongated squall lines), consistently with findings of Morrison (2016a, b). Nicholls et al. (1991) derived separate expressions for the two geometric flow patterns. In recent work, Groot and Tost (2023b) identified the significance of the differences in idealised LES of different convective systems. In essence, this results in a variability in the amount of upper tropospheric divergence away from a convective system at the cloud top.

The divergence variability is governed by the combination of either quasi-two-dimensional or quasi-three-dimensional vertical overturning (or a mixture of those) and, herewith connected, the morphology of organized convective systems. In the current

study, we examine whether variability in outflow strength from realistic convective systems in NWP may be explained by the same concepts.

110

A major step forward in Convective organisation

One of the mechanisms that can organise convection is actively driven by gravity wave dynamics (e.g. Mapes, 1993; Lane and Reeder, 2001

115

. The propagation velocity of gravity waves is inversely proportional to their vertical wavelength (e.g. Grant et al., 2018). A metric for the vertical wavelength is the count n of wave crests over twice the vertical depth of the troposphere. In this

metric waves with $n = 1$, $n = 2$ and $n = 3$ are nearly always or usually fast enough to propagate away from the convective system, in the analysis of the evolution of flow perturbations in this century has been achieved from a atmospheric dynamics point of view. A strong (initial) connection of variability growth with (convective) precipitating systems has become obvious (e.g. Zhang, 2005; Zhang et al., 2007; Selz and Craig, 2015a, b). With the help of the potential vorticity perspective, narrow initial condition spread could reveal this link directly (Selz et al., 2022; Baumgart et al., 2019; Rodwell et al., 2013). However,

120

such cases are from a practical perspective currently improbable due to the mostly larger initial state uncertainty. Nevertheless, this uncertainty will pertain and propagate in all situations. It introduces the growth of flow perturbations due to scale interactions (which may cascade both upscale and downscale in practice (Lorenz, 1969; Durran and Gingrich, 2014)). Despite, improvements can be utilised to further reduce uncertainty on small scales (Selz et al., 2022; Zhang et al., 2019).

125

presence of a typical background flow. These first few vertical modes of propagating gravity waves create regions of preferred upward motion and of preferred positive / negative temperature perturbations in the lower and upper troposphere. The perturbations from the background state thereby increase / reduce the tendency of deceleration of upward moving parcels in certain layers (i.e. convective inhibition (CIN)) and modifying the convective available potential energy (CAPE); see for instance Adams-Selin (2020a), Figure 6). As the gravity waves propagate (also) horizontally, conditions can alternate between more and less favourable conditions for the initiation of deep convection (compared to the background state). Consequently, moving spatial patterns of locations favourable and unfavourable for convective initiation occur around pre-existing convective systems.

130

Baumgart et al. (2019) have investigated the sequence of dynamical processes that (on average) contribute to mid-latitude growth of flow perturbations. They proposed that latent heating tendencies from their deep convection scheme in ICON may induce differential divergent winds. As gravity waves simultaneously impact the spatial distribution of convective updrafts and downdrafts and are generated by heating (cooling) signals produced in updrafts and downdrafts, complicated mutual interactions can occur (e.g. Groot and Tost, 2023a, b; Houze, 2004; Adams-Selin, 2020a, b; Grant et al., 2018). These interactions may disturb the simple but typical point sources of divergence and convergence resulting from gravity waves emitted by a local latent heating maximum. The conceptual model proposed by Groot and Tost (2023b) provides an explanation: as divergent winds of convective clouds appear in the form of wave signals, the waves may collide in the upper troposphere. Subsequently,

135

further non-linear growth of flow perturbations in the upper troposphere is driven by differential advection. A key question is whether the variability in flow perturbations is comparably (and reliably) represented in simulations with resolved and parameterised deep convection. A latent heating conditional perspective on convectively induced flow variability is taken in this study. The analysis from the conditional perspective will be compared to results obtained with an LES model and the

140

consistent idealised gravity wave outflow magnitude (Groot and Tost, 2023b; Nicholls et al., 1991). Furthermore, indirectly, a pathway via which organised convection could play a role in processes of perturbation growth may be identified. This role of organised convection for flow perturbations has been suggested by e.g., Rodwell et al. (2013) and Clarke et al. (2019b, a). Therefore, convergence may occur locally upon collisions of the wave signals at cloud top levels (Figure 1), which presumably closes the upper tropospheric divergence budget over larger scales (Groot and Tost, 2023b; Nicholls et al., 1991). It is thought that this interaction causes a non-linear response of divergence to increasing latent heating. Other mechanisms, like vertical wind shear, cold pool propagation and (related) moisture convergence also impact the organisation and clustering of convective systems. These mechanisms may interact with the gravity wave dynamics that (co-)organises the convection. In this work it is not of relevance which mechanisms cause convective organisation and aggregation, but it is important to be aware that those factors interact. A comprehensive review of convective organisation and relevant mechanisms is provided by Muller et al. (2022).

Furthermore, convective momentum transport (CMT) can may modify upper-tropospheric flow perturbations induced by deep convection (Rodwell et al., 2013). Rodwell et al. (2013) found that mesoscale convective systems over the North-American continent could affect European weather predictability. CMT may not only play a crucial role in the organisation of convective systems, but also in downstream perturbation development. Groot and Tost (2023b) noted that the effect of CMT could be separated into a direct and an indirect effect: firstly, CMT affects divergent flow and associated horizontal acceleration directly, resulting in flow perturbations around convective systems. Secondly, as CMT affects the convective organisation and precipitation rates, this results in an indirect modification of upper-tropospheric flow. A direct effect on divergent outflows was not identified in LES (Groot and Tost, 2023b), possibly due to too weak upper-tropospheric shear. In this study, the direct effect of CMT on divergent outflows from deep convection will be assessed for ICON simulations.

The missing – but crucial – modelling strategies that complement idealised models like the linearised model and idealised LES, from which physical understanding of processes could be gained, will be examined in this study. Bridging the gap to operational NWP (ICON 2.6) is a step towards a (very) basic understanding of divergent deep convective outflow magnitudes across a broad range of simulation set-ups. Meanwhile, the relationship between net latent heating and divergent convective outflows in the upper troposphere is assessed in a realistic, but also complex setting. Both parameterised and explicitly resolved deep convection are used: thereby, potential limitations of the parameterised treatment of deep convection may be exposed. In Groot and Tost (2023b) a linear relation of outflow strength to net latent heating was found, with superposed variability induced by outflow dimensionality. Altogether, the following (LES-inherited) hypotheses will be tested on convection-permitting ICON simulations

Analysis and hypotheses

The following hypotheses are investigated here:

- The dimensionality of convective systems substantially affects the magnitude of divergent outflows. In case of divergent outflow from isolated convective cells compared to the outflow of convection closely resembling a line. Geometry of a convective system is statistically related to divergent outflow strength, where updrafts approximately in line produce comparatively less divergent outflow than those that resemble a point source of heating (e.g. elongated squall lines), a

contrast in ratio between divergence and latent heating is expected: at the same area mean intensity of latent heating, less divergence is expected for a linear geometry than for a corresponding point source. at given heating rates (as in Figure 1a versus b)

- Convective aggregation and organisation affects the magnitude of divergent outflows – the outflow is expected to increase at a rate slower than linearly when convective aggregation leads to increases in the mean precipitation rate (probably partly explained by adjusting the outflow dimensionality). While convective systems aggregate, grow upscale and organise, the precipitation rate tends to increase, but the ratio between mass divergence and precipitation rate decreases on average (compare Figure 1a to 1c)
- Variability in CMT does not affect the magnitude of divergent outflows from deep convection and hence normalised convective momentum transport does not have a statistically significant relation with the normalised alter the typical (i.e. mean) ratio between mass divergence and precipitation rate, as found by Groot and Tost (2023b).

To assess the above hypotheses, convective systems are tracked in Furthermore, it will be investigated whether comparable effects on mass divergence variability are represented in ensembles with parameterised moist deep convection. Nevertheless, representation of such effects would not be expected in the first place, since convective organisation is represented in a much more simplified way in convection parameterised simulations than in convection-permitting ICON. The relationship between net latent heating and the magnitude of divergent outflow from deep convection in the upper troposphere is evaluated based on the findings by Groot and Tost (2023b). Hypotheses are tested using an ellipse fitting algorithm to assess the elongation of convective systems (a concept used before by Grant et al. (2020) and references herein), with validation procedures to assure consistent parameter evolution. Furthermore, convective systems that resemble an elongated squall line are examined in convection-permitting simulations. Squall lines resemble line setups. The methodology will be detailed in Section 3.2.1.

Therefore, we firstly investigate if sub-linear increases of mass divergence occur at increasing precipitation rates (corresponding to latent heating rates) in convection-permitting and convection parameterised ICON ensembles of a single event. The event is exemplary and will demonstrate whether the methodology is useful, as well as indicate first conclusions on whether the conceptual understanding is likely correct and represents dynamical feedbacks of convective aggregation in state-of-the-art NWP at mid-latitudes. Another aim is to investigate whether patterns resembling line and point sources may be separated using our proposed methodology. If both of the leading aspects of storm morphology, resulting from line and point sources of heating better than other convection. In the parameterised convection set-up variables are integrated over a box volume in various simulations, with a set-up similar to Groot and Tost (2023b). Hereby, it is chosen to not track the systems. Diagnostics are integrated over a one-hour window for each convective system instead (motivated in Section 3.2.2). on the one hand and convective organisation and clustering on the other hand, are connected to the divergence variability, simulation setups are able to represent gravity wave interactions and the impact of storm morphology on upper-level divergence patterns. Supposedly this is possible at 1 km grid spacing, but not at 13 km resolution, when convection is parameterised.

The manuscript is organised as follows: after a short synoptic discussion of the simulated case (Section 2), the model and simulation configuration is described in In Section 2, the investigated event is characterised in terms of synoptic conditions. In

Section 3, including an example track of a convective system and corresponding evolution of the parameters of an ellipse-fitting algorithm (Section 4) the simulations and the data-analysis methods are described. Subsequently, Section 4 illustrates the key parameters derived from the simulations output by discussing their evolution in an exemplary convective system. Then, the upper-tropospheric (250 hPa) divergence variability among convective systems in parameterised convection deep convective outflow strength is compared between convection-parameterised and convection-permitting ensembles is assessed in relation to the location of convective features in Section 5.1. Subsequently, the divergent outflows are compared between parameterised convection and ICON in Section 5.2. In Section 6, we analyze the convection-permitting simulations (Section 5.2). This is followed by an assessment of the three hypotheses presented above in Section 6 for convection-permitting simulations. Subsequently, a synthesis and discussion section is presented (Section 7). ICON by characterizing the relation between key parameters and the strength of divergent deep-convective outflows. Thereby, the representation of deep convection during the event is investigated following the hypotheses formulated in this introduction. Afterwards, we reflect on the results and their coherence in the discussion of Section 7, as well as their implications. This is followed by the main conclusions (Section 8).

225 2 Synoptic conditions of the case study

The organised convection over Central Europe on June 10th and 11th is notorious for the Munich Hail Storm (Wilhelm et al., 2021). An upper-tropospheric low pressure system was located over Western France on June 10th 2019 (Figure 2; grey isolines with geopotential height patterns), with a southerly flow advecting warm, moist air northward over Central-Europe (high θ_e , red). The associated pattern with cold air west of the upper low pressure system led to strong baroclinicity over France, the Alps and (later) Germany. Cold surface air creeping northeastward directly ahead of the collocated cold front supported the initiation of strong convective systems. These systems are present in nearly all simulations, albeit at slightly different locations than in reality, including east of the front in the region of warm near-surface air. Storms generally appeared further to the west in the convection-permitting ensemble and even more so in the parameterised set-up than in reality.

After all, several systems with mesoscale convective activity developed over Germany and the Alps during the afternoon and evening, which were co-located within the parameterised deep convection ensemble. Similarly, convection was relatively active in convection-permitting simulations over Southern-Germany in the (late) afternoon of the 10th of June (e.g. Figure 7a; observed convective systems are also shown there). Well organised convection occurred over regions with strong relief in the southwest. In the east initially surface-based convection occurred in the late afternoon to early evening. The strong south to southwesterly upper-level flow helped to organise convection in convection-permitting simulations to a varying degree: a few convective systems in the east of Southern-Germany developed squall line-like structures. On the contrary, other structures only organised into smaller multicells. This mixture may be very suitable for assessments of divergent outflows from deep convection, since idealised LES simulations suggest that convective organisation, geometry and aggregation may be crucial aspects for the outflow. These aspects determine the normalised outflow strength with respect to net latent heating (Groot and Tost, 2023b). A more detailed discussion of the synoptic configuration and actual convective evolution around this event is

250 hPa Isotachs at 30-35-40-45-50-55-60 m/s, 250 hPa height
 Equivalent potential temperature at 600 hPa
 12 UTC + 10h, 10-06-2019

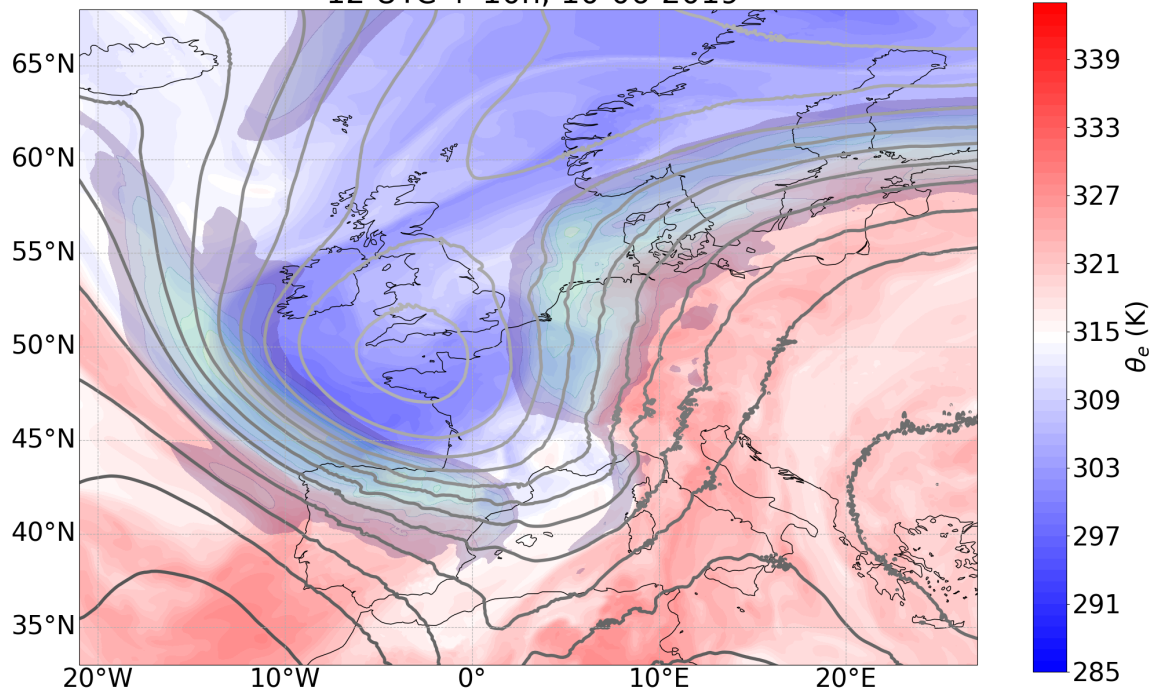


Figure 2. Equivalent potential temperature at 600 hPa (blue-white-red), isotachs at 250 hPa (30 to 60+ m/s at 5 m/s intervals, transparent colors) and geometric height of the 250 hPa surface at ca. 11 km height and with 50 m intervals forecasted for 22 UTC on June 10th over Western Europe.

245 provided in Wilhelm et al. (2021).

3 Methods

3.1 Model set-up

3.1.1 Domains, grids and ~~parameterizations~~parameterisations

250 This study investigates numerical simulations with ICON 2.6 (Zängl et al., 2015; Giorgetta et al., 2018), which is developed and operated by the German Weather Service and Max Planck Institute for Meteorology. Simulations have been conducted and analysed in the following configurations:

- Global simulations, with a nest over Europe ("PAR")

– Convection-permitting simulations over Southern-Germany ("PER") using the local area mode (LAM)

255 The PAR-simulations have been initiated at 12 UTC on June 10th 2019, whereas PER-simulations over Southern Germany have been initiated at 03 UTC [on the same day](#) (Figure S1 in the Supplement). For details on simulation settings, see Table 1. We refer to Prill et al. (2020) for the mostly similar default parameterisation settings.

Table 1. Simulation settings within the three domains.

Domain	Global domain	European Nest	LAM, Southern Germany
Model version	2.6.0		2.6.2.2
Grid spacing (km)	26 (R03B06)	13 (R03B07)	1 (R05B09)
Time step (s)	100	50	10
Domain top altitude (km)	75		22.5
Number of vertical levels (-)	90		90
Deep convection parameterisation	Tiedtke (1989), Bechtold et al. (2014)		None
Time step deep convection (s) and subgrid orography	1200	600	
Time step gravity wave drag (s)	1200		
Microphysics parameterisation	1M (Seifert, 2008)		2M (Seifert and Beheng, 2006)
Radiation parameterisation	Ritter-Geleyn ¹		RRTMG
Time step radiation (s)	1800		600
Grid spacing radiation (km)	52	26	1
Rayleigh damping height (km)	22		12.5
Initial conditions	DWD analysis		KENDA, provided by Matsunobu et al. (2022)
Initial condition time	12 UTC		03 UTC
Initial condition set	Deterministic		20 member ensemble
Ensemble perturbations	Surface dataset ($n = 6$; 2015-2018)		Initial conditions
Boundary conditions	None (two-way nested)		ICON EU ensemble forecasts (20 km)
Additional perturbed simulations (number)	Rescaled: - Latent heating $\pm 5\%, \pm 10\%, \pm 20\%$ (6) - CMT tendencies (none, $\pm 50\%$) (3) Deep convection scheme: - No parameterisation (6, ensemble perturbations) - Adjusted calling frequency (2)		None
Output time step (min)	None	10	5
Total integration time (hours)	33		16

3.1.2 Ensemble and perturbation settings

260 Ensembles have been used with the aim to sample an unspecific form of background convective variability within a similar large-scale flow configuration. To further sample the variability ~~of the PAR-set-up, additional~~ experiments with adjustments ~~to the default PAR-set-up following Groot and Tost (2023b)~~ have been done ~~, essentially matching Groot and Tost (2023b)~~ (Table 1). Global nested simulations have been perturbed with alternative surface tile ~~dataset, datasets (outdated, spanning various dates over 2015-2019)~~, whereas the 20 member ICON-PER initial condition ensemble closely resembles the operational ICON D2-ensemble of DWD.

The combined variability imposed by selecting various convective systems over a time range and through the dimension of ensemble members allow allows us to study the characteristics of convective variability in a precipitation-conditional framework.

The results presented will mostly be focused on the comparison of the PAR and PER ensemble and on the PER ensemble itself.

270 3.2 Extracting convective system properties in ICON simulations

~~Extraction of convective system properties~~ For a fair comparison, the divergence in convection-permitting simulations are low-pass filtered, whereby the variability in the wind field at scales up to 45 km is removed using a discrete cosine transform. Thereby, the convection-permitting and convection-parameterised simulations obtain roughly the same effective resolution in the divergence field. Therefore the divergent outflows are well intercomparable and there is no problem of small-scale divergence patterns in convection-permitting simulations (lacking in the parameterised configuration).

275 Extraction of properties of individual convective systems (shape, area, etc) can be achieved in the PER-simulations. On the contrary, parameterised treatment does not lend itself very well to such an extraction procedure, because it assumes that a statistically averaged effect of convection over larger scales exists and is represented (e.g. Done et al., 2006). Therefore, any description of (sub-grid) variability induced by convective cells and convective organisation is represented less accurately than
280 in convection-permitting simulations with finer grid (if at all represented). The extraction procedure of organised convective systems and associated metrics from the PER-simulations is described in section 3.2.1, followed by discussion of metrics from PAR in 3.2.2.

3.2.1 Convection-permitting simulations “PER”

~~It is important that the~~ In order to single out the expected outflow regime (2D-like or 3D-like), the dataset with properties of convective systems ~~is must be~~ able to describe the degree of convective aggregation clustering, orientation and the relative state of elongation of convective systems in time and space ~~(similar to a dimensionless number)~~. ~~Consequently, it is possible to single out whether an almost 2D or almost 3D outflow regime can be expected~~. These factors have been found to determine the relative magnitude of outflow from deep convection ~~(Groot and Tost, 2023b)~~. ~~To estimate parameters~~ (Groot and Tost, 2023b, and Figure 1). Parameters describing the elongation and state of aggregation for any convective system ~~are estimated with~~ an ellipse fitting algorithm which has been designed ~~for this purpose (Figure 3, blue boxes at the~~

top). In parallel, ~~an independent a~~ moving box is initiated to track a convective system ~~. The independent box is needed to~~
~~conserve~~ (Figure 3, red arrows towards the red box). The box conserves a moving integration volume, relative to the convective
system's main updraft, over which divergence and precipitation rate are integrated. ~~The~~ After the independent boxes have been
determined, the following steps lead to a dataset of convective systems and ellipse parameters:

- 295
1. Ellipse fitting ~~A moving box is initiated to track each convective system in a simulation~~
 2. Ellipse fitting (blue boxes no. 1-4 in Figure 3)
 3. Validation and ordering of obtained ellipse parameters (blue boxes no. 5-6 of Figure 3)
 4. ~~Construction of precipitation rate, filtered mass divergence and convective momentum transport diagnostics~~
 5. ~~Moving box integration of the constructed diagnostics along a convective system's track~~

300

 6. Matching between ellipse parameters and moving box diagnostics, as obtained from a specific convective system and
that specific simulation (brown arrow and first brown box at the bottom of Figure 3)
 7. Final check of the matched records (second brown arrow at the bottom of Figure 3)

~~The full procedure is explained below. Before the ellipse fitting and validation procedure is detailed, the following two~~
~~paragraphs describe the procedure to derive box diagnostics.~~

305

~~Ellipse fitting is applied to any area larger than about 400 km² with a precipitation rate over 10 mm/h in PER-simulations. Before fitting the ellipses, a binary representation of convective precipitation is smoothed spatially (\sqrt{r} dependence) over a 20 km radius. Subsequently, an initial validation procedure assesses the stability of the ellipse parameters over a one-hour window. Short-lasting very strong fluctuations are filtered out. Only fluctuations that match any prior and successive record within~~
~~one hour are maintained (Groot and Kuntze, 2023). Note that the corresponding prior or successive records might have been~~
~~incidentally removed by this procedure. Removal of each independent record is possible: at least one plausible predecessor~~
~~and successor of each validated record has to exist in this step, both forward and backward in time. Additional validation~~
~~measures check the distance between an ellipse center (set to be < 20 km) and a convective system's track, identified with~~
~~an independently moving box. A list of ellipse parameters extracted in the procedure is provided Table A1 (Appendix).~~Box
315 volumes

~~Independently from ellipses, a moving box has been initiated subjectively and moves with a convective system. The box is used~~
~~for integration of precipitation and divergence over a horizontal subspace that is constant in time (with respect to the moving~~
~~box centre). The convective systems propagate with relatively constant velocity north- or northeastward and only 1-3 systems~~
~~have been tracked in each simulation (see also Figure 5-17a). Manually defined boxes moving at a constant velocity could~~
320 therefore be used to define ~~the box outlines. The moving boxes are initiated and then track the systems independently from the~~
~~ellipse fitting procedure, because merging events (such as between smaller satellite ellipses and larger ellipses) occur frequently~~

in the ellipse dataset. In case of a merging event, ellipse parameters will weakly vary in time, but the spatial integration mask of the moving box should not change accordingly. If ellipse parameters vary strongly, the validation procedure is not passed. The signal of divergence and precipitation within a box should predominantly be affected by the main, central convective system within the box and only be weakly affected by satellite systems that develop from time to time around some of the systems.

325 integration outlines.

For each box and time step the following variables are calculated: Firstly, the strength of convective momentum transport (CMT) is computed to determine whether and how this acceleration (deceleration) affects the upper-tropospheric divergence. The estimate of CMT is based on the eddy covariance of perturbations ($'$) in u, v, w cross-correlation products of flow deviation vectors ($u' = u - u_{mean}, v', w'$) from the domain mean values. Separate estimates of the meridional and zonal correlations with vertical velocity representing (resolved, vertically-integrated) convective momentum transport fluxes are made at vertically integrated up to model level 25 :(located at 315 hPa or about 9 km altitude). This level is selected, because the eddy flux in the upper troposphere turns out to be mostly maximal troposphere has a maximum at or near this level during the studied event. The box mean values of $u'w'$ and $v'w'$ represent the vertical integral of CMT acceleration over all levels below the selected

330 level. Both CMT and divergence are normalised with respect to mean surface precipitation, i.e. a proxy, proxies of box mean latent heating (into quantities from here on called C for normalization of CMT and D for normalization of mass divergence), to investigate the connection between anomalies in both quantities (conditioned on precipitation rate) in a more robust way. Secondly, the mean precipitation intensity and the filtered mean divergence (wavelengths > 45 km in both horizontal directions; variability at short wavelengths removed; top parts of Figure 3) is computed. These three quantities can only be computed if

340 the whole box lies within the extent of the simulation output at any given time. box is fully contained within the simulation domain.

The moving boxes are initiated and then track the systems independently from the ellipse fitting procedure, because merging of ellipses occurs frequently in the ellipse dataset. In case of a merging event, ellipse parameters will weakly vary in time, but the spatial integration mask of the moving box should not change accordingly. If ellipse parameters vary strongly, the ellipses

345 cannot be validated. The signal of divergence and precipitation within a box should predominantly be affected by the main, central convective system within the box and only be weakly affected by small/shallower neighbouring cells that develop from time to time around some of the systems.

Ellipse fitting and constraining the final PER-dataset

350 Ellipse fitting and verification are used to quantify geometry of convective systems, in line with Grant et al. (2020). However, a new methodology tailored at our hypotheses is developed. The ellipse fitting is applied to any area larger than about 400 km^2 with an average precipitation rate over five minutes exceeding 10 mm/h in PER-simulations (blue box no. 1). Before fitting the ellipses, a binary representation of convective precipitation is smoothed spatially (\sqrt{r} dependence) over a 20 km radius

355 (blue boxes no. 2-3 in Figure 3). A module named CV2 (as part of OpenCV, utilized in 2022) is used for the ellipse fitting procedure, and for the technical details, we refer to the code (Groot and Kuntze, 2023). Subsequently, after fitting ellipses,

an initial validation procedure assesses the stability of the ellipse parameters over an one hour window (next boxes, no. 4-5, Fig. 3). Short lasting very strong fluctuations are filtered out. Only fluctuations that match any prior and successive record within one hour are kept (Groot and Kuntze, 2023). The result is a track of each convective system, which may contain one or more gaps of one or several time steps (blue box 6, Figure 3).

Subsequently, after integrating the precipitation rate, divergence and convective momentum transport spatially (red arrows and boxes), additional validation measures check the distance between an ellipse center (set to be < 20 km) and the corresponding box center (first brown arrows in the center of Figure 3). A list of ellipse parameters extracted in the procedure is provided Table A1 (Appendix).

Finally, the ellipse characteristics of the ellipses contained within each box (elongation A : length ratio between two ellipse axes; O orientation; area of the ellipses) are then-matched with the corresponding records-averaged-integrated divergence, CMT and precipitation rate as computed over the moving box -volume. It should be noted that the ellipse parameters and the corresponding box-integrated diagnostics are matched within one simulation and for one specific convective system within that simulation. An example of the path of a moving box and (contained) ellipses with corresponding ellipse parameters for one convective system is provided in Section 4.

Dataset

The ellipse dataset fulfilling all conditions of quality control contains 456 records, in which the time evolution of 22 of a total of 28 convective systems is represented (following the validation procedure). This dataset is the basic dataset for the assessment in Sections 5.2 and 6. With a slightly weaker box-center-to-ellipse-center distance criterion, a second dataset of 866 records is obtained. For this larger dataset, the distance criterion was set individually for each convective system (based on e.g. characteristics such as box size) or replaced with an ellipse area criterion. In the larger dataset, all 28 convective systems are present. Since the validation algorithms turned out not to be fully failsafe, ambiguous records-In a few cases, duplicates fulfill all validation criteria based on area and centre location of the ellipse at one specific time stamp. Duplicates have manually been selected before finalising both datasets: 5 additional matches were ambiguous (duplicates fulfill all validation criteria at one specific time stamp)-five additional duplicates were in the dataset of 866 (+5)and 2 of those; two occurred in the dataset of 456 (+2) records. The double matches among those ambiguous records were manually selected (removed) based on area and centre location of the ellipse.

3.2.2 Convection parameterising simulations "PAR"

In past times, computationally-Computationally feasible NWP resolutions required-require the application of a parameterisation to represent deep convection, although mostly just in current global models. Only recently, global convection-permitting simulations have been utilised for research purposes (e.g. Judt, 2020) (and even in such a setup, shallow convection is often parameterised).

The philosophy behind the representation of deep convection is and has been generally different between parameterised convection and convection-permitting simulations approaches - for simulations with parameterised deep convection:

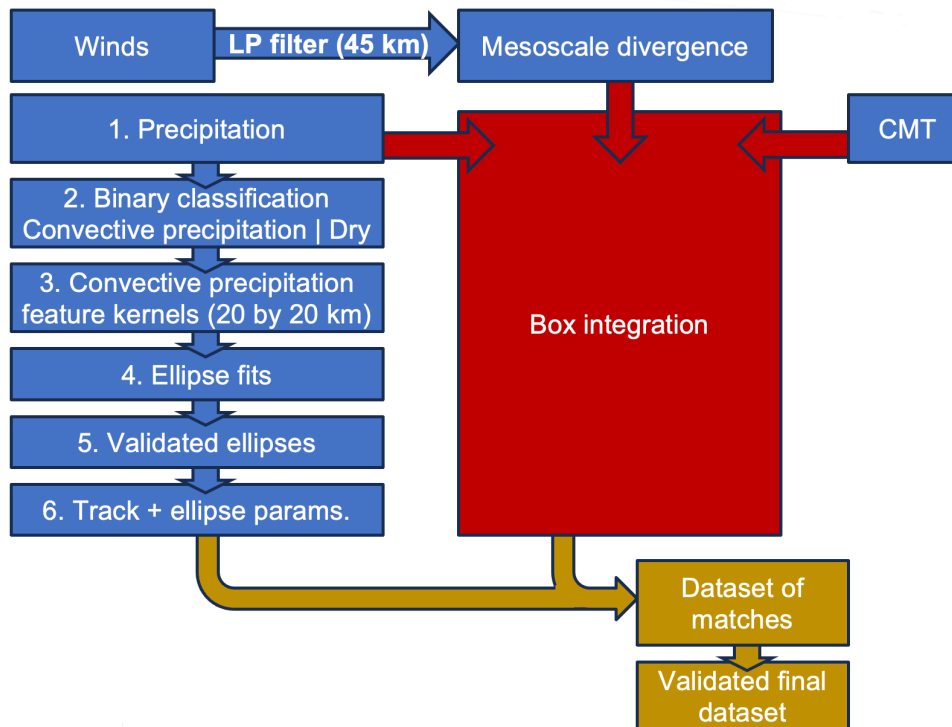


Figure 3. Processing of the raw ICON PER simulation data to obtain the dataset used in the analysis of section 4 and onward. The input fields displayed in the four blue boxes at the top. The pre-processing steps, numbered 2-6, are also displayed in blue boxes. They consist of three parallel streams of data, derived from precipitation rate, eddy flux of CMT and filtered divergence and serve as inputs to the box area/volume integration (which itself is displayed in red). These streams merge into a dataset of the precipitation rate, divergence and momentum transport (CMT) and ellipse parameters. A match occurs based on center distance between ellipse centre and box centre at a given time. The ellipse records and box records can merge in the first brown arrow's step if the distance is under a threshold (main processing step 2), followed by another final verification step of post-processing before a dataset is fixed for final use in this work. These steps are further detailed in section 3.2.1.

The workflow as documented here is carried out by scripts published in Groot and Kuntze (2023).

- Convective cells are not advected with the background flow, but have their full life cycle within a cell: there is a split between [larger-scale, explicitly represented](#) dynamics and the parameterisations [of subgrid-scale motion \(including deep convection\)](#) in each grid cell (Lawrence and Salzmann, 2008; Prill et al., 2020)
- An equilibrium assumption is done (e.g. ~~Done et al., 2006~~) (e.g. [Done et al., 2006](#); [Becker et al., 2021](#)), where (deep) convection represents the adjustment mechanism of the atmosphere to the presence of static instability. Adjustment occurs under the condition that convection can be triggered. ~~Grid~~ However, [grid](#) cells in numerical models are [often](#) so

small nowadays that the equilibrium, between convective forcing and the adjustment on a ~~separated~~separate scale, is questionable.

400 – The temporal resolution of the full life cycle of convection within an individual cell is either represented within a full time step (typically in climate models), or the adjustment process and reduction of CAPE takes place over several consecutive time steps.

As a consequence, the representation of deep convection by parameterisation does not only tend to smoothen precipitation through its coarser resolution, but also through underestimated spatial and temporal variability (Keane et al., 2014) .

405 Even though there ~~is~~are small differences between the assumptions applicable to different convection schemes (Arakawa, 2004), ~~arguments the assumptions outlined~~ above and the comparatively large grid size imply that convective organisation is not directly represented in simulation ~~set-ups configurations~~ with parameterised deep convection. ~~Categorisation through~~ Therefore, categorisation by convective organisation is ~~poorly (if at all) hardly~~ justifiable (see also Satoh et al., 2019). Consequently, an application of a complex tracking algorithm following parameterised deep convective systems is not suitable. A statistical sample of convective cells technically regenerates anyway, while ~~a corresponding precipitation displaces itself over~~ a corresponding precipitation moves together with conditionally unstable or lifted air ~~mass masses~~.

410 Furthermore, the LAM-domain is small (400 by 500 km), whereas the parameterised convection simulations cover ~~Europe most~~ parts of Europe with a grid spacing of 13 km. A typical (mesoscale) convective system is easily contained within a box of several to tens of grid cells in each horizontal direction for ICON-PAR. Therefore, three static boxes are chosen and compared among the PAR-simulations. These boxes are ~~set-up designed~~ such that the dominant precipitation and divergence signals associated with convective systems fall within the boxes, ~~as needed~~. Three very different deep convective systems are systematically compared across six ensemble members.

4 Example of a track in ICON-PER

The track of one of the two convective systems in ensemble member 14 of the PER simulations is illustrated in Figure 4a. The box centre is indicated as a red line, with bi-hourly markers along the way. The first snapshot at 12:30 UTC shows that the ellipse algorithm detects an aggregated convective system at the edge of the box. This large system does not fully fall into the box. The validation procedure automatically reports a failure (represented by an X) because of a too large distance between the box centre and the ~~convective system~~ellipse centre (which is surrounded by the convective system).

425 Subsequently During the next hours, small convective cells develop near the center of the box (14:30 UTC). The easternmost system obtains a surrounding ellipse located within close range of the box centre. Another one to the west also obtains an ellipse, but the distance to the box centre is larger. Therefore the latter match is rejected.

Two hours later, again two matches are found: one very near the box centre and one to the north of the centre, but within the box. The larger central one matches through the distance rule, but the northern one gets rejected.

At 18:30 UTC, an elongated convective system develops in association with the earlier central system (14:30, 16:30 UTC).

Still sitting close to the box centre, it is the only ellipse within the box.

430 In Figure 4b the evolution of the ellipses over short time intervals is illustrated. The differently colored precipitation and box features move to the northeast slowly. However, the ellipses undergo various changes, which is associated with a slight convective reorganisation. The reorganisation is induced by new cell formation in a close proximity of the older system. The northeastern feature is detected throughout, but blue crosses demonstrate that the match is initially rejected. The box is slowly closing in on the system, as revealed by the possible match (square marker) at the sixth and last time step. For the southwestern
435 system, the initial system (larger purple ellipse associated with it) breaks up into smaller pieces for two successive time steps and eventually disappears. One of the ellipses of the southwestern system (blue circle) matches with the box at one instance (green), when the ellipse is closest to the box centre.

However, the northeastern system matches at just one instance: the last time step. This match is only valid for the larger dataset with relaxed conditions. This illustrates how convective (re-)initiation and small displacements can affect the ellipse parameters.

440 Corresponding jumps in evolution of ellipse parameters are filtered out. The wobbly interval is indicated by the dark ~~red outline~~ purple rectangle at 17:30-18:00 UTC. Most ellipses in this interval are rejected due to ~~such behavior~~ wobbly ellipse parameters, but some are retained during the interval. A temporary shrinking in the axes lengths is seen (without consequent rejection in the validation), due to the stability criteria and interpolation from any ~~neighbouring prior and successive~~ records within an hour. Another jump within the time window is seen in the offset parameters (Figure 5). Nonetheless, the ~~general behavior evolution~~ of ellipse parameters is mostly smooth over the five hours. ~~The behavior~~ This evolution illustrates that the regenerating systems
445 can successfully be detected, covering ~~its~~ their temporal evolution.

The evolution of upper-tropospheric divergence, CMT and precipitation rate over the moving box is found in the supplement (Figure S3). Around 13 UTC no records of the system are validated: the validation criteria haven not been fulfilled (green solid outline in Figure 5).

450 Between 14 and 15 UTC two convective systems have been matched with the box (Figure 4). One is travelling at a distance of about 20 grid cells from the box centre and the other at about 4-9 cells (10-20 km).

The distance between the centre of an ellipse and the associated convective box centre is maximum 9 grid cell distances (20 km) for the strict dataset of 456 records (purple line versus pink ~~dashed outline~~ solid rectangle in Figure 5).

5 Intercomparison of divergent convective outflows in ICON-PER and ICON-PAR

455 The representation and variability of convective outflows in ICON-PER and ICON-PAR ensembles is compared here. In particular, the mean mass divergence over moving boxes and in corresponding areas of persistent thunderstorm activity is investigated. First, the spatial-temporal characteristics of divergent outflows are broadly assessed for the selected systems in both ICON-PER and ICON-PAR. This provides a basis for the quantitative intercomparison of divergent outflows between both configurations, for which we condition on the precipitation rate (equivalent to net latent heating rate). Case-related information
460 on the convective organisation and plausible assumptions on the outflow characteristics are used to further characterise the dataset.

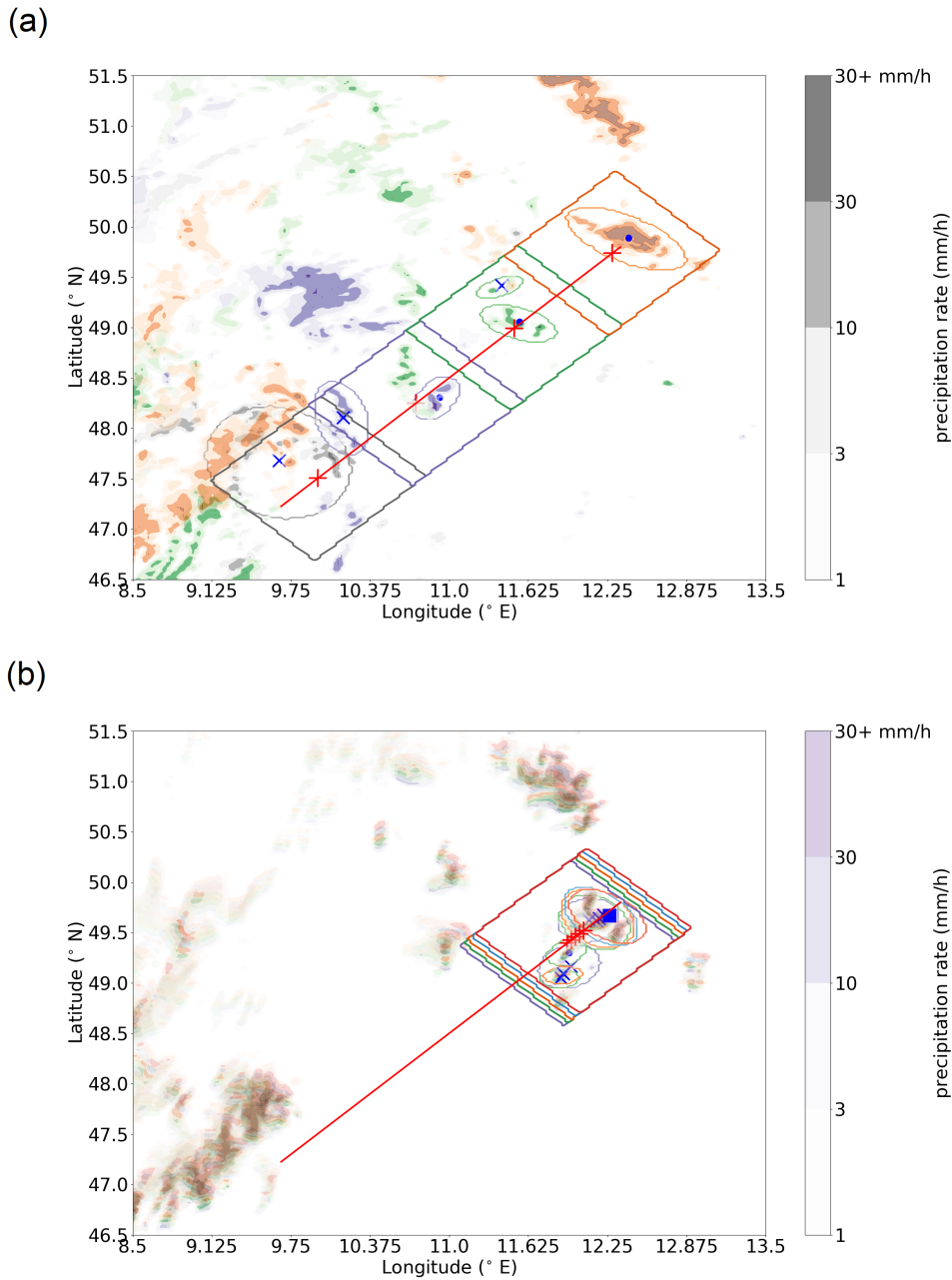


Figure 4. Precipitation rate (mm/h) in ensemble member 14 of the PER simulations at (a) 12:30 UTC (grey color scale), 14:30 UTC (purple), 16:30 UTC (green) and 18:30 UTC (orange). The color intensity represents precipitation rate according to the color bar shown for 12:30 UTC. Same Same for 17:30-17:55 UTC with 5 minute intervals (b). The box outline (tilted rectangles) designed to track the convective system is displayed in the same color. The edges of ellipses matched with the box outline are also indicated. The track of the box with time is indicated by a red line and its centre location is indicated by a +. The distance from that red plus-sign to the ellipse center (blue markers) is evaluated and marked with an x for distances larger than 11 grid cells (about 25 km), a blue circle for those within 20 km and a blue square for those at 20-25 km distance.

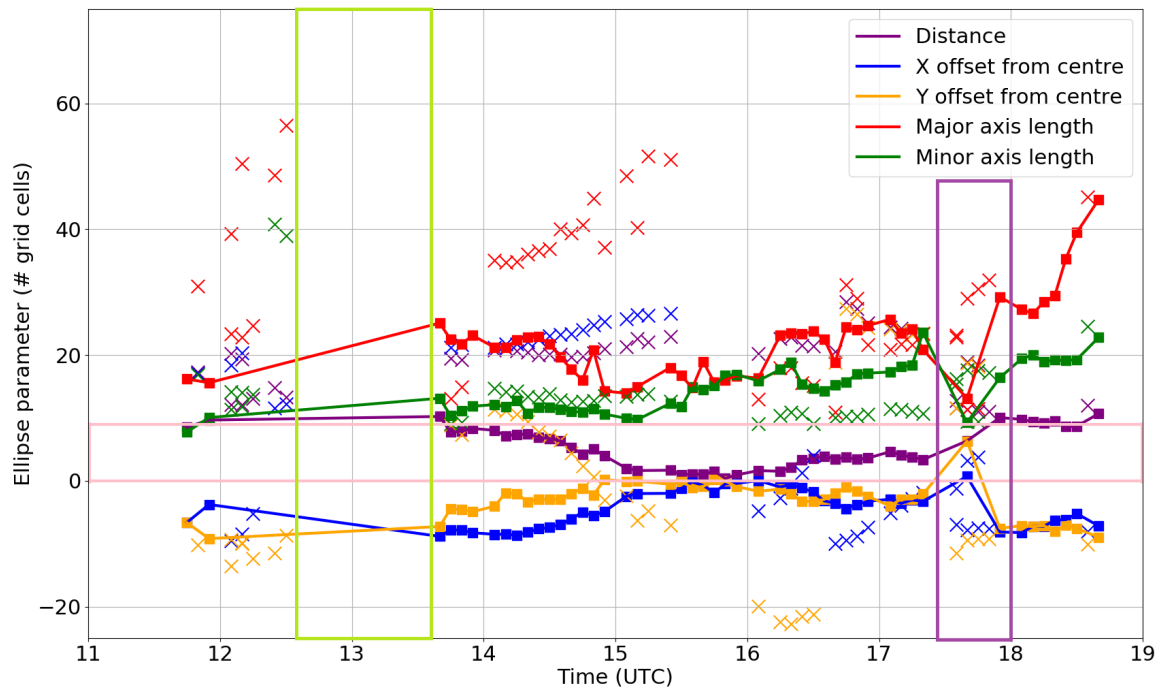


Figure 5. Example of time evolution of ellipse parameters in the dataset for the same convective system as shown in Figure 4, halfway through the validation process. Different colors indicate various ellipse parameters. Red: Major axis length, green: minor axis length, purple: distance from box center (+ in Figure 4); blue and orange: offset in x- and y direction from box center). Crosses represent rejected ellipse records for any of the final datasets. Square markers with a line indicate accepted records. The subset within the pink dashed outline indicates the presence of a record solid rectangle defines which records are in the small subset of 456 records.

After this comparison, Section 6 will analyse the upper tropospheric mass divergence versus precipitation rate and the corresponding ellipse parameters (ICON-PER only; this is motivated in the current section), which is a verification of the conceptual understanding presented in the introduction (e.g. Figure 1).

465 5.1 Convective systems and associated patterns in divergence (variability)

Figure 6 depicts the evolution of the vertical profile of horizontal divergence averaged over 28 convective systems in PER, although at no point in the evolution all 28 systems are simultaneously present. The time evolution of the median levels of neutral divergence of the systems is shown by the black dashed lines, with grey dashed lines representing the The time evolution of mean horizontal divergence over the moving boxes in ICON-PER is displayed in Figure 6. Boxes without deep convective activity have been omitted. Furthermore, the boundary between mass divergence and mass convergence has also been highlighted. The evolution of upper and lower quartiles of the distribution pressure level of this boundary has been marked by a grey dashed line, while the median is added in black. Inflow of deep convection Deep convective inflow (mass convergence)

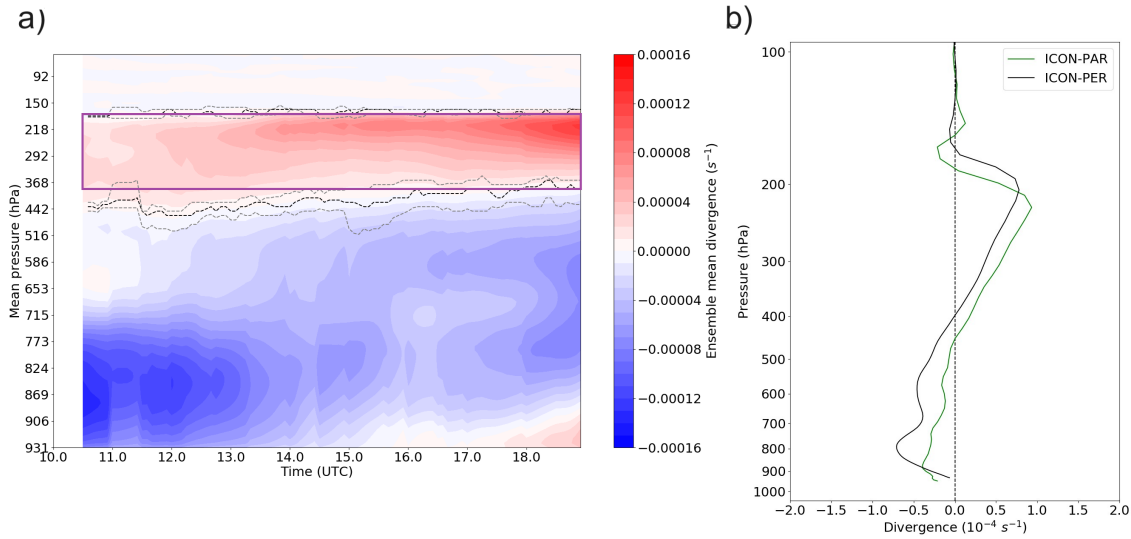


Figure 6. (a) Evolution of mean-box-mean divergence (convergence) along the-track-of-28-convective-systems-tracks, as a function of mean pressure. Note that at each instance only a subset of the 28 convective systems will-actually-be-is active. Black dashed lines indicate the median level of neutral divergence at any time and grey dashed lines the corresponding 75th and 25th quantiles (nearest to the vertical maximum of divergence). The solid purple outline indicates the levels between which the divergent outflow has been integrated in PER. (b) Mean vertical divergence profile over the last seven hours of panel (a) (ICON-PER), as well as for ICON-PAR across the analysed systems and ensemble members.

predominantly occurs in the boundary layer (931-to-bottom boundary up to about 800 hPa~~mean pressure~~) initially. Subsequently, the convection tends to become elevated (16-19 UTC) in ICON-PER, dominated by inflow at ICON-PER: dominant
475 inflow levels lift to about 600-800 hPa. Furthermore, inflow and entrainment Furthermore, weaker inflow, and entrainment,
typically occurs up to about 450 hPa. Above this level the 400-450 hPa (roughly the boundary between net convergence and
divergence), the main outflow region extends upward. A strong vertical gradient in the mean divergence is found around 180-
190 hPa, close to the tropopause. Near to this level, many convective systems have another level of neutral divergence, i.e., the
upper boundary of the divergent outflows in ICON-PER (as expected).

480 PAR-profiles also reveal a strong divergence maximum directly underneath/beneath the tropopause (see supplementary material:
Figure Figure 6b and Figure S5). The levels in the supplement), just below the 200 hPa level. The typical level of neutral diver-
gence at the tropopause occur at altitudes similar to those found in explicitly simulated convection is shifted downward by about
15-20 hPa compared to ICON-PER. However, the variability of the lower level of zero divergence, between 500-550 and 350
hPa, is-increased-increases when utilising a deep convection parameterisation in our case (see also Figure S5). Furthermore,
485 the mean lower bottom level of the divergent outflows is located about 50 hPa lower in ICON-PAR than in ICON-PER.

According to Figure 6, the maximum of mass divergence occurs between 200 and 300 hPa. The spatial variability of horizontal
divergence for ICON-PAR and ICON-PER ensembles is illustrated in Figure 7 b-d at about 250 hPa (i.e., within the layer

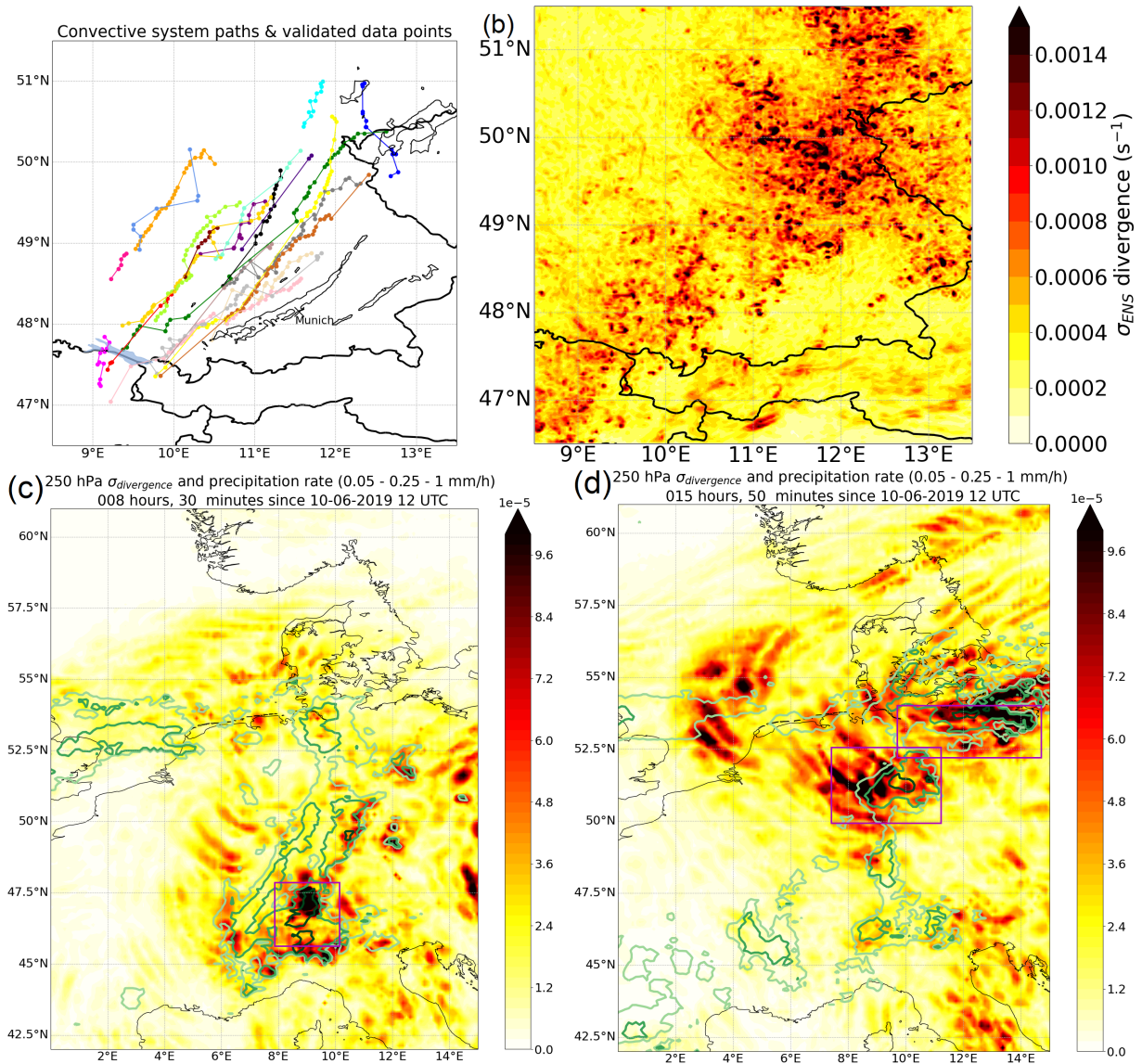


Figure 7. (a) Paths of convective systems over Southern-Germany as included in the dataset of 456 records for ICON PER. In black contours, tracks of observed convective systems with > 55 dBZ reflectivity are shown for the same day, which generally appear further to the southeast than those in ICON. The color shading in b-d shows the ensemble standard deviation of the divergence σ_{ENS} . (b) σ_{ENS} at 255 hPa and the 10th of June 2019 18:00 UTC for ICON-PER. (c-d) σ_{ENS} at 250 hPa and the 10th of June 20:30, resp., (e-d) (11th of June 3:50 UTC (d)), both for ICON-PAR. Isolines in light green to dark green indicate precipitation intensity over 0.05, 0.25 and 1 mm/h (ensemble mean; bottom plots); the boxes surrounding three convective systems are outlined in purple.

approximately the level of maximum divergence) in ~~Surface precipitation rates of ICON-PAR and ICON-PER ensembles, in combination with surface precipitation rate are also shown.~~ Figure 7a shows the tracks of ~~22 of~~ the convective systems (as derived from the ellipse dataset) passing over southern Germany in PER. ~~These~~ The convective systems generally move from southwest to northeast through the domain. ~~As only a subset of the records were validated, straight sections without markers can occur along tracks for rejected ellipses. Few systems move northward (e.g., the initially easternmost system). Generally, the precipitation systems tend to increase their intensity and size with time—correlation coefficients between output time and system intensity-area are 0.22, 0.25 respectively (see also Figure 11).~~ Furthermore, their mean intensity increases gradually over time (as manifested by their cross-correlation coefficient with time; as to be shown later, in Figure 11 of Section 6). While the overall mean precipitation rate over the moving boxes is 3.1 mm/h, the value increases to 4.4 mm/h between 17:30 and 19:00 UTC. Furthermore, the average position of the box centres moves toward the northeastern quadrant of the simulation domain in the last 1.5 hours, ~~which is also the region coincident~~ with the largest ensemble variability in ~~the 255 hPa divergence overall upper level mass divergence~~ (Figure 7 a). ~~The~~ Summarised, the large variability in the divergence is associated with the proximity of increasingly active convective systems.

Results for PAR simulations are shown in Figure 7c and 7d for two different simulation time steps: maxima in upper-tropospheric divergence variability are again co-located with enhanced convective precipitation. However, not all regions with (strong) precipitation are directly connected to enhanced upper-tropospheric divergence variability. One possible explanation ~~for a weaker relation~~ may be the release of latent heat ~~substantially below 250 hPa~~ predominately at lower tropospheric levels, which would lead to divergence in the middle instead of the upper troposphere (within the regions with surface precipitation and no or weak upper-tropospheric divergence variability). Another reason for weak connectivity are overall small deviations from the ensemble mean, both in precipitation rate and mass divergence. ~~Furthermore, ensemble mean precipitation rates smoothen spatial maxima of individual members.~~

In Figure 7 the convective system over the Swiss Alps (9°E, 47°N, panel c) and those over Northern-Central Germany (51°N, 10°E and 53.5°N, 12°E, panel d) are the regions dominating divergence variability. Consequently, rectangular boxes (purple) define the integration mask for the following analysis.

5.2 Comparison of relationship between net latent heating and outflow divergence in ICON-PER and ICON-PAR

Figure 8 shows the relation between outflow mass divergence and precipitation rate in all of the analysed ICON-simulations. ~~Records~~ (Note that we switch to mass divergence units from now on, since Figure 7b, c and d showed divergence at a fixed pressure level (i.e. nearly constant densities on that level), whereas from here on vertically integrated values are used. The line of low D corresponds to the slope of highly organised squall lines in an LES-study, which approaches the limit of 2D convection from Groot and Tost (2023b). Only records ($n = 456$) with validated ellipses are included (in Figure 8a). Furthermore, the temporal evolution of three separate convective systems that eventually develop into squall line-like structures are highlighted by colored symbols(see Figure S5 of the supplement for their distribution of precipitation rate)In particular, these highlighted points correspond to the part of their evolution, during which squall line-like development gradually occurs. Note time in general increases with increasing precipitation intensity. These systems are thought to resemble two-dimensional

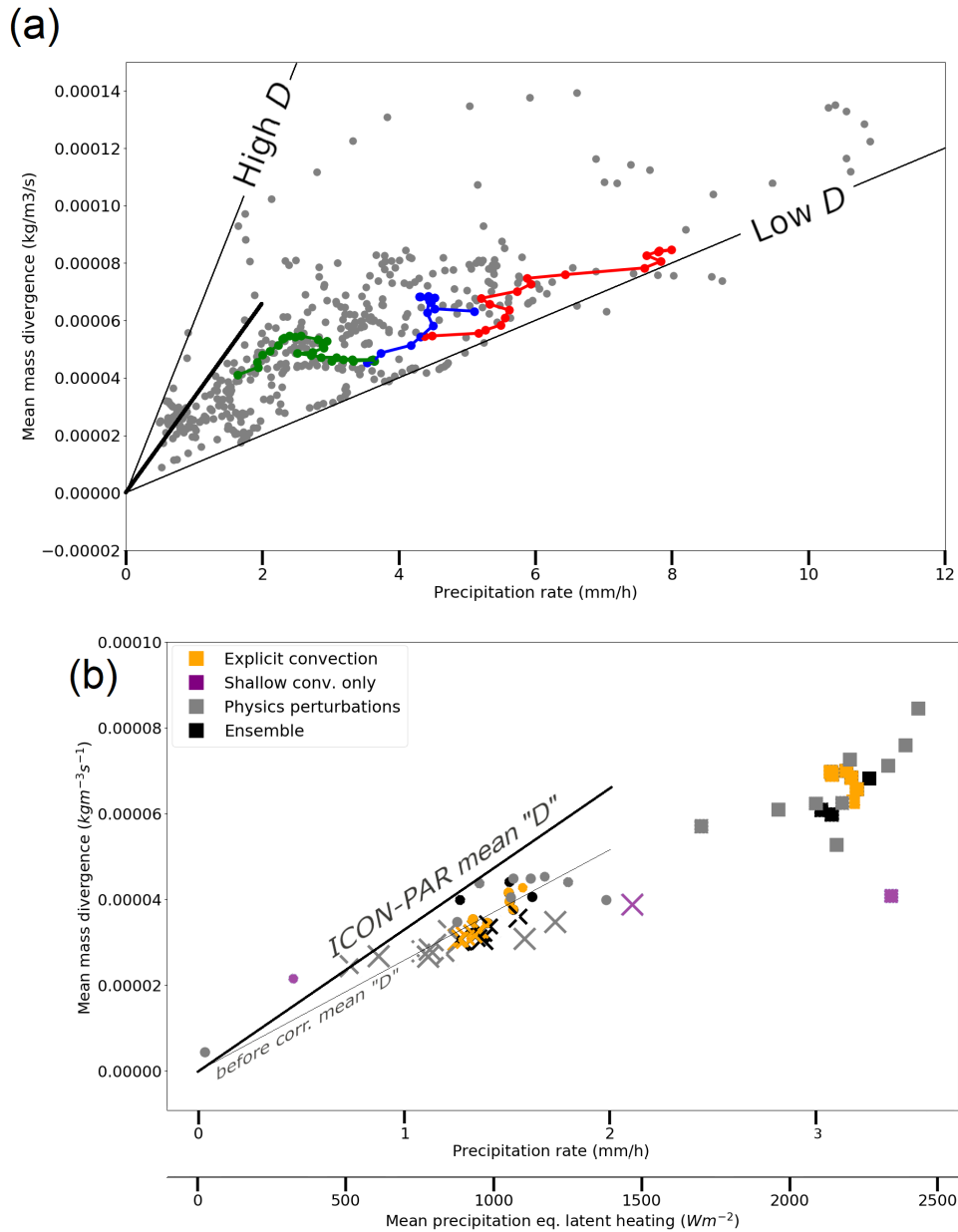


Figure 8. (a) [Divergence-latent Divergence-precipitation rate relationship \(convertible to divergence-column net latent heating relationship\)](#) for ICON-PER-simulations in the validated dataset of 456 records (grey), plus the time evolution of three convective systems that form a short squall line in three ensemble members (colors). Divergence is integrated over the 380 to 180 hPa layer. (b) Same relation integrated over model levels from 420-430 hPa up to 175 hPa for ICON-PAR (black: ensemble and parameterisation calls at lower frequencies; grey: perturbed latent heating or convective momentum transport; orange: no deep convective parameterisation; purple: shallow convection parameterisation only). In (b), three different markers correspond to three different convective systems, which correspond to the three purple boxes of Figures 7c and 7d.

[In both panels, the mean value of quantity "D" \(ratio of mass divergence and precipitation rate\) based on ICON-PAR is also annotated as bold black line, and both before and after correction for the difference in outflow layer thickness in the bottom panel b \(before the correction: thin black line; see annotating text of b\).](#)

convection much closer than isolated three-dimensional-like systems. ~~The three colored lines show the precipitation rate and divergence of these three systems in the stage of squall line-like development. Time increases with increasing precipitation intensity (towards the right).~~

525 The ratio between mass divergence and precipitation rate effectively represents the normalised mass divergence D (if the intercept at 0 mm/h corresponds to 0 divergence, which is a reasonable assumption for cumulonimbus clouds, but this assumption does not hold for the non-precipitating stages of clouds). Our hypotheses and the conceptual model (Figure 1 and the accompanying paragraphs of Section 1) suggest that this ratio is not expected to be constant over time, unless the convective overturning remains either two-dimensional or three-dimensional as a result of constant geometry of the convective system. Hence, when
530 noise is removed, the time evolution of a convective system in the "precipitation rate"- "divergence" space is expected to correlate with the change in convective overturning as a result of changing convective organisation. If a squall-line-type of organisation develops, the geometry is gradually expected to become increasingly two-dimensional. Accordingly D should become rather low (at least when systems developing squall-line-like characteristics are separated from the sample mean of D). Therefore, we expect that systems while developing squall-line-like characteristics gradually move towards lower D as the
535 systems grow and their precipitation rate increases. In the following, we regress the mass divergence with the precipitation rate for the three selected systems, to assess whether this hypothesis is true.

Figure 8a shows that, while squall line structures develop (colored lines), D (i.e., normalised divergence) ~~moves towards indeed~~ moves towards typically lower values over time. Consequently, mass divergence becomes comparatively low compared to a fitted mean mass divergence at a given precipitation intensity taking all data points into account. ~~The slope between mass~~
540 ~~divergence and precipitation rate effectively represents the normalised mass divergence, namely D (if the intercept at 0 mm/h is 0 divergence, which is a reasonable assumption for clouds, but would be rather invalid for a non-precipitating stage of the clouds).~~ For the green system with lowest precipitation intensities, the slope of ~~the a~~ a linear least squares fit ~~is negative. As a result of this slope with respect to precipitation rate, it moves to its evolution in the precipitation rate - mass divergence space is negative. Therefore, it develops~~ (in the diagram) towards a low normalised divergence, while squall line-like structures de-
545 velop. The fit to the evolution of the other two systems in the precipitation rate - mass divergence space (blue and red markers) have a positive gradient with respect to precipitation rate has a positive slope, as typical for the background scatter. However, the intercept of the linear fit at 0 mm/h precipitation rate lies below the intercept value representative of the background fit (see Table 1 in the Supplement for the intercept and slope parameters of the linear fits). Therefore, these systems are at low-lower
 D than the background, too. Furthermore, ~~one could see~~ Figure 8a suggests that for the latter two systems the gradient of mass
550 divergence with precipitation rate seems to decrease, decreases as precipitation rate increases ~~(with time and, i.e. over their lifetime and the increasing resemblance to a squall line-like developments) structure~~. The propagation of these squall line-like systems towards lower than expected D at a given precipitation rate in Figure 8a fits the expected impact of dimensionality type of outflow source on convective outflows (Groot and Tost, 2023b): namely that systems that resemble line sources of heating emit gravity waves causing reduced divergence at the same heating rates, compared to point sources (corresponding
555 to isolated cumulonimbus updrafts). In Section 6 we will further investigate if the variability in ratio D within the ICON-PER dataset aligns with the conceptual model of Figure 1. First, the corresponding character of the variability within the ICON-PAR

dataset is discussed and then compared to ICON-PER.

The PAR-simulations, illustrated in Figure 8b and representing three different convective systems as marked with crosses, squares and dots, suggest a roughly linear relation between mass divergence and net latent heating. If neutral divergence is assumed in the layer excluded from the vertical extent of PER-integration masks, PAR and PER can be compared, even though the integration depth differs by about 50 hPa between the two ~~-(about 200 vs. about 250 hPa pressure thickness).~~ The expected impact, based on an assumption of neutral mass divergence in layers excluded from the analysis, would translate to a $\approx 25\%$ stronger outflow in PER. Based on ~~the this~~ assumption, the corrected mean PAR-divergence would ~~be higher than the correspond with a steeper slope in the Figure than the slope of the regression line of PER-divergence for agiven surface precipitation rate.-D~~ in ICON-PER. The corrected and uncorrected sloping lines from ICON-PAR are illustrated in Figure 8b, while only the corrected line of ICON-PAR is visualised in 8a. Hence, a direct visual comparison between PAR and PER is possible.

~~Enhanced~~ On average, enhanced outflow occurs in PAR compared to PER at given net latent heating rates. The relationship for unperturbed parameterised deep convection (black, Figure 8b) appears to be very close to linear, as little or no information on ~~mode of organisation, such as the geometry of the convective systems can be represented with a parameterisation (see also Section 3.2.2).~~ The appearance of a squall line structure ~~, is considered with the parameterisation approach (Section 3.2.2), is missing; precipitation structures of such a squall line would not be convective and would closely resemble the dynamics of tilted lifting, as typically associated with a frontal zone (see Appendix C2 of Groot, 2023).~~ The relationship is also linear for the ensemble without any convection parameterisation (orange). If only shallow convection is parameterised (magenta markers), the outflow of one system deviates substantially from the linear relationship, ~~as a result of a.~~ This can be explained by a considerable downward shift of ~~outflow levels, the outflow layer. Consequently, the integration mask as defined in Figure 6 misses the dominant levels of convective outflow, as the outflow is redistributed from upper levels towards mid-levels.~~

In short Figure 8b suggests that the coarse resolution linearises the precipitation rate-outflow relationship and that the ~~deviations are generated by cloud-scale dynamical features~~ spread is only represented at higher convection-permitting resolution, in ICON-PER, presumably by representing refined cloud heating, which results in gravity wave emission and dynamical interactions between these gravity waves. Furthermore, physical perturbations in the parameterised configuration cause only slight deviations from ~~the seemingly this approximately~~ linear relationship. ~~Such a behavior~~ The detection of minor conditional outflow spread (when conditioned on heating rates) agrees well with expectations from the absence of convective organisation in parameterised convection. Explicitly ~~resolving~~ "resolving" deep convection at 13 km grid does not affect the suggested linear relationship. On the other hand, in convection-permitting simulations at 1 km horizontal grid spacing the latent heating-outflow ratios vary. The envelope of variation is roughly consistent between ~~ICON-PER and idealised CM1 simulations (Groot and Tost, 2023b).~~ The study and references herein indicate that an envelope with variable mass divergence per unit latent heat release is probably the most realistic representation. ICON-PER and the idealised LES-simulations of Groot and Tost (2023b).

As there are no systematic patterns of a residual outflow-net latent heating relationship obvious in the ~~PAR-ICON-PAR~~ simulations, the analysis of such patterns is restricted to the ICON-PER configuration in Section 6.

6 Dependence of divergent deep convective outflow on properties of convective systems in convection-permitting ICON simulations

595 This section discusses the representation of divergent convective outflows in ICON-PER, following the conceptual model outlined in the introduction and then discussing the role of CMT. The conceptual model in the introduction suggests that divergent outflow strength depends

- linearly on net latent heating rate (hence, also on precipitation rate)
 - on the storm geometry (point or line heating source)
 - on interactions between outflows from individual convective cells as a result of convective clustering, through outflow collisions
- 600

The main diagnostics used in this section are: (i) the ratio D between mass divergence in the upper troposphere and the corresponding net precipitation rate (see Table A1) and (ii) the ratio C between the eddy momentum flux and precipitation rate. In addition, we use ellipse parameters to describe the geometry and mean-flow relative orientation of the convective elements.

605 6.1 Elongation of convective systems

The elongation of convective systems is quantified by the ~~axis-ratio A between the two ellipse,~~ which is defined by the ratio of two axes of the fits ellipses fitted to the convective systems. ~~One would expect an on average~~ From the LES study and the conceptual model of Groot and Tost (2023b) lower A is expected for systems with a ~~low divergence to precipitation rate ratio~~ lower D , at a given precipitation rate (Groot and Tost, 2023b). Furthermore, during the evolution of a convective system A is expected to correlate positively with D . Finally, for two-dimensional convection it is expected that the convective inflow and outflow are mostly parallel to the tropospheric mean winds, resulting in a typical ellipse orientation O perpendicular to these winds.

610

The dataset of precipitation and divergence shown Figure 9 suggests that low A generally corresponds with low D at high precipitation intensities (> 6 mm/h). However, at low precipitation rates ~~the axes ratio classes are more mixed. At low precipitation intensities~~ no clear relationship between A and D is ~~detectable~~ found. This suggests that the elongation of convective systems is not the only parameter accountable for anomalies in the ~~outflow strength-latent heating~~ "outflow strength" - "latent heating" space. The classification into three A -classes can be sensitive to thresholds of A , but Figure 9 shows that sorting of A and D is not supported at low precipitation intensities.

615

~~Contrasts are nevertheless present when generating subsets of the simulation data first to all precipitation intensities above 2.5~~ The ellipse dataset is split in subsets for further investigation. After selecting the subset with > 2.5 mm/h and then to two classes precipitation rate first, within this subset, two subsets of strong D anomalies (at least $\pm 15\%$ from are created: one subset that exceeds 115% of the conditional mean of quantity D); Larger D ("low D " class) and another where $D_{sample} < 0.85 \times D_{con.mean}$ ("high D " class). The "high D " class is associated with an average A of 0.602, versus 0.542 for low D the "low D " class (see

620

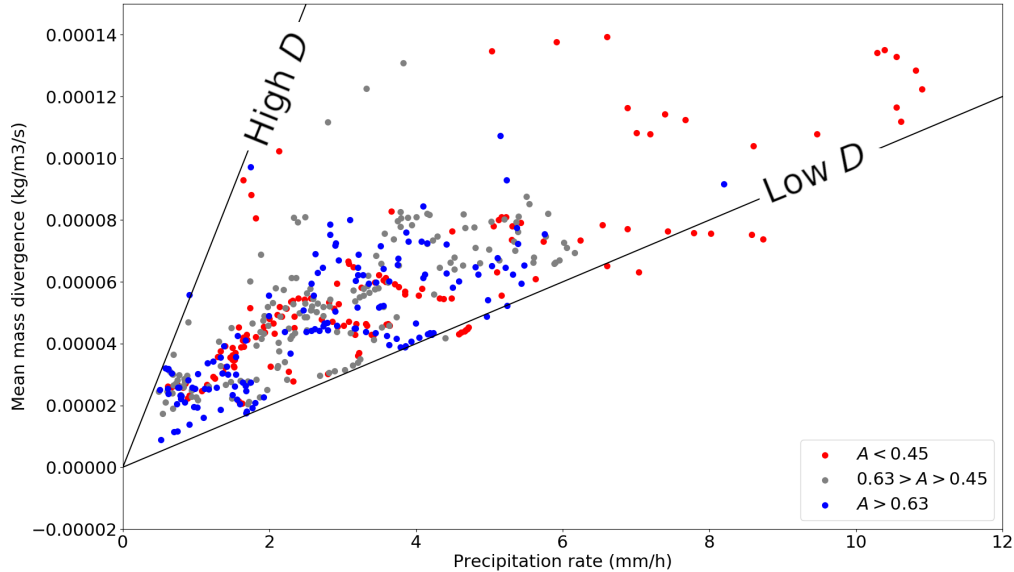


Figure 9. Divergence-precipitation dataset in ICON PER simulations with colors indicating three similarly sized classes of axes ratios. Added are two black lines of constant D : those with $6e-5 \frac{kg \cdot mm}{m^3 s^1 h^1}$ and $1e-5 \frac{kg \cdot mm}{m^3 s^1 h^1}$.

also [Table B1, Appendix B](#)). The mean value over the whole dataset is 0.56 with σ of 0.18. Therefore, the difference of the
 625 expected ([i.e. positive](#)) sign is significant at 95% confidence. Nevertheless, the difference in A between the classes is lower
 than expected based on Groot and Tost (2023b).

Furthermore, variability in ellipse orientation O within the low D [class-subset](#) is strongly reduced compared ~~to instances with~~
[with the](#) high D [subset](#): $\sigma = 32^\circ$ for low D versus $\sigma = 44^\circ$ for all records and $\sigma = 45^\circ$ ~~degrees~~ for the high D subset. ~~This~~
~~corresponds to comparatively~~ [In short, very](#) similar ellipse orientations ~~with reduced variance~~ ([reduced variance in ellipse](#)
 630 [orientation](#)) occurs at low normalised divergence D ([Table B1, Appendix B](#)).

6.2 Aggregation of convective systems

Figures 8a and 9 suggest a deviation from the linear relationship towards larger precipitation rate, i.e. reduced D for con-
 vective systems with increasing precipitation rates. ~~Therefore, mass divergence is non-linearly related to precipitation rate in~~
~~the convection-permitting ICON ensemble, in contrast to simulations at coarser resolution (Figure 8b).~~ [In this subsection,](#)
 635 [we quantify the off-linearity of the relationship between mass divergence and precipitation rate, which has been found for](#)
[ICON-PER, but not for ICON-PAR.](#)

A reduction in mass divergence may be caused by the collision of individual three-dimensional outflows from individual cells,
 as induced by convective aggregation. Hence, convective aggregation may reduce divergence, relative to isolated convective

cells, as more precipitation cells develop within an area. ~~Measures that indicate developing and aggregating~~ Measures that can indicate the presence of developing and clustering convective systems are ellipse area and area ~~over which a precipitation threshold of 10 of high (> 10 mm/his exceeded)~~ precipitation rate (Table A1 in the Appendix; Figure 11). Furthermore, precipitation intensity itself generally increases with an increasing number of mature precipitation cells, ~~simultaneously increasing convective aggregation within a respective area in a small area, also an indicator of convective clustering.~~

The expected negative correlation of the amount of mass divergence per unit precipitation intensity D with increasing size and (precipitation) intensity of the convective systems is found in the dataset (11). The most important relation connects precipitation intensity and the ratio D with a Pearson correlation coefficient of -0.59 in the fully validated dataset and -0.52 in the larger dataset ($n = 866$). The negative correlation bends off the scatter in Figure 9 towards lower divergences than in case of a continued linear relationship (like in Figure 8b).

The robust negative correlation coefficient between D and precipitation rate implies the non-linear behavior within the envelope of Figure 9 is partially predictable: a non-linear best fit between divergence and precipitation rate is expected. A power law with power < 1 could optimally fit the relation between mass divergence and precipitation rates. Indeed, a best fit for the smaller dataset is obtained with an exponent of 0.704. ~~Applying a transform with that power to precipitation rates, the best divergence prediction is obtained in terms of least squares.~~ The lowest least squares residual to predict the divergence from precipitation rate uses this exponent. For the larger dataset, the exponent is 0.606. With bootstrapping the uncertainty in the transformed fit of the smaller dataset is investigated. The 95% confidence of the power transform was estimated at 0.526 to 0.851. However, since multiple highly correlated parameters contribute to the fit (intercept, slope, exponent), the actual parameter uncertainty is likely smaller.

Conditional correlations between the ellipse area and D are evaluated within precipitation bins ~~also support the signal of convective aggregation. These.~~ These correlations support the representation of convective clustering and its consequences for outflow collisions within ICON-PER, consistently with LES (Groot and Tost, 2023b). The conditional correlations are summarised in Figure 12: the (sample size) weighted mean correlation coefficient is -0.32, which is significant at 95% confidence. Furthermore, the area > 10 mm/h precipitation rate reveals the same pattern, with a weighted mean correlation coefficient within precipitation bins of -0.29.

The analysis suggests the following evolution of the convective characteristics: increasing precipitation intensity forces a linear increase in mass divergence in the upper troposphere, initially. However, beyond a certain precipitation intensity the mass divergence does not keep up with the initially linear relation anymore. At higher precipitation rates mass divergence tends to grow comparatively slower (i.e. negative feedback). This signal was exemplified by the developing ~~squall line-like~~ squall line-like structures in Figure 8a. The non-linear divergence reduction is stronger in squall line-like structures than in the average of all sampled convective systems. These convective systems move towards the right lower corner in Figure 8a.

In the supplement (Figure S6) surface-based and mixed/elevated convection subsets are analysed separately, where a fingerprint of convective aggregation is present, too. ~~Overall, the non-linearity in mass divergence suggests that the expected impact of convective aggregation on D is present within the PER-dataset. Furthermore, the impact of convective aggregation is qualitatively consistent with idealised LES (Groot and Tost, 2023b).~~

6.3 Role of convective momentum transport

675 For the larger dataset with less strict matching criteria, the effect of convective momentum transport on mass divergence has been investigated by normalising both quantities with the precipitation rate (C and D) and analysing conditional correlations of C and D within precipitation rate bins. Thereby, the first order effects of precipitation intensity on mass divergence (Section 6a,b) are filtered out. Figure 10a shows zonal (x-axis) and meridional (y-axis) components of CMT, while Figure 10b shows the relation between quantities C and D over two separate ranges of precipitation rate. The precipitation rate bins to
680 diagnose the conditional correlations are constructed such that the ratio between upper and lower bound of ~~the precipitation rate bins~~ each precipitation rate bin is about 4 to 5 and ~~covers the~~ the combination of all bins cover the interval 0.6-6.25 mm/h (Figure 12).

Over the 11 bins containing 39-150 samples each, the weighted average of the conditional correlation coefficient is 0.31. The equal weight average is 0.34, ~~with~~. There are exclusively positive correlations with values up to 0.7-0.8 ~~within~~ across the range
685 of bins. Given these statistics, the true correlation coefficient lies probably ~~on~~ within the interval 0.2-0.5. Therefore, a small fraction of outflow variability in the convective systems can probably be explained by variability in CMT (Figure 10b).

No single data point with upgradient transport occurs within the dataset (Figure 10a), since the CMT-fluxes oppose the predominantly southerly wind shear vector of this event, hence reducing the vertical gradient in the wind speed, and therefore, the wind shear. The sample of 866 records is not fully independent, as only 28 independent convective systems are represented
690 with records at small time lags being correlated. The temporal evolution of several convective systems in a single synoptic environment is of course somewhat biased towards a specific scenario. On the other hand, the coherent background flow supports identifying subtle patterns in the dataset. This contrasts strongly with the experimental method in Groot and Tost (2023b) to study CMT effects on mass divergence.

7 Synthesis

695 7.1 ICON representation of divergent outflows

7.2 **Summary**

This study has investigated divergent outflow variability from deep convection in ICON, conditional on the precipitation intensity. ~~Both ensembles of parameterised (PAR; $dx = 13$ km) and explicitly resolved convection (PER; $dx = 1$ km) have been analysed for one event in ensembles with convection-parameterised (PAR) and convection-permitting (PER) setups.~~
700 ~~Prominent flow variability in the upper troposphere co-locates with convective outflows in both PAR and PER (Figure 7). This analysis suggests that deep convection can be an important source of flow variability in the upper troposphere early in simulations, consistent with Baumgart et al. (2019). PAR-simulations show a highly an approximately linear relationship between net latent heating and the outflows precipitation rate (a close proxy for vertically integrated latent heating rate) and the outflow strength~~ with little spread. Conversely, in PER a non-linear relation between ~~precipitation rate and upper-level~~

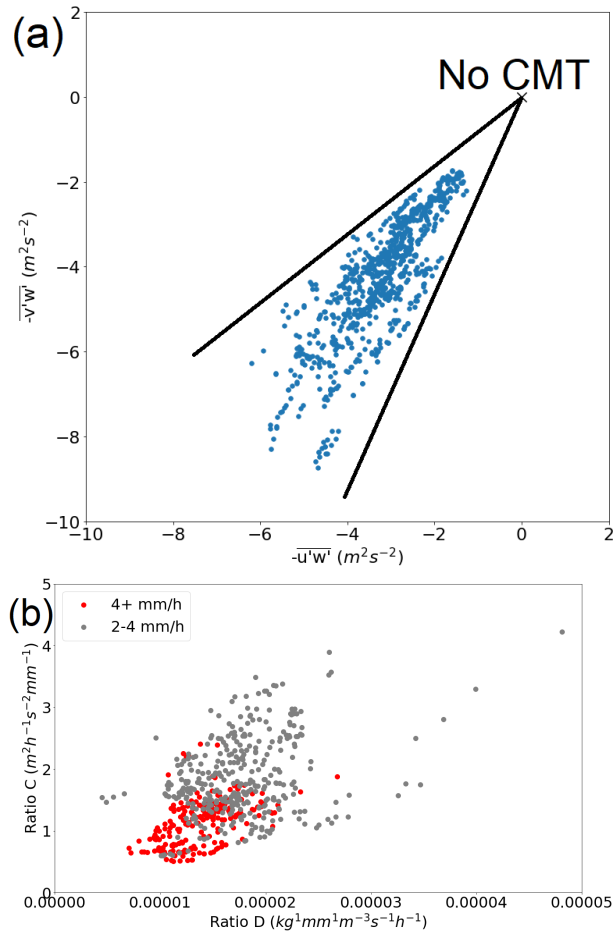


Figure 10. Top (a): two components of the diagnosed vertical CMT integral at 315 hPa (overbar denotes mean operator). Bottom (b): relation between upper-tropospheric mass divergence and the absolute acceleration derived from the CMT diagnostic, both normalised to precipitation rate and for two different classes of precipitation rates (red and grey).

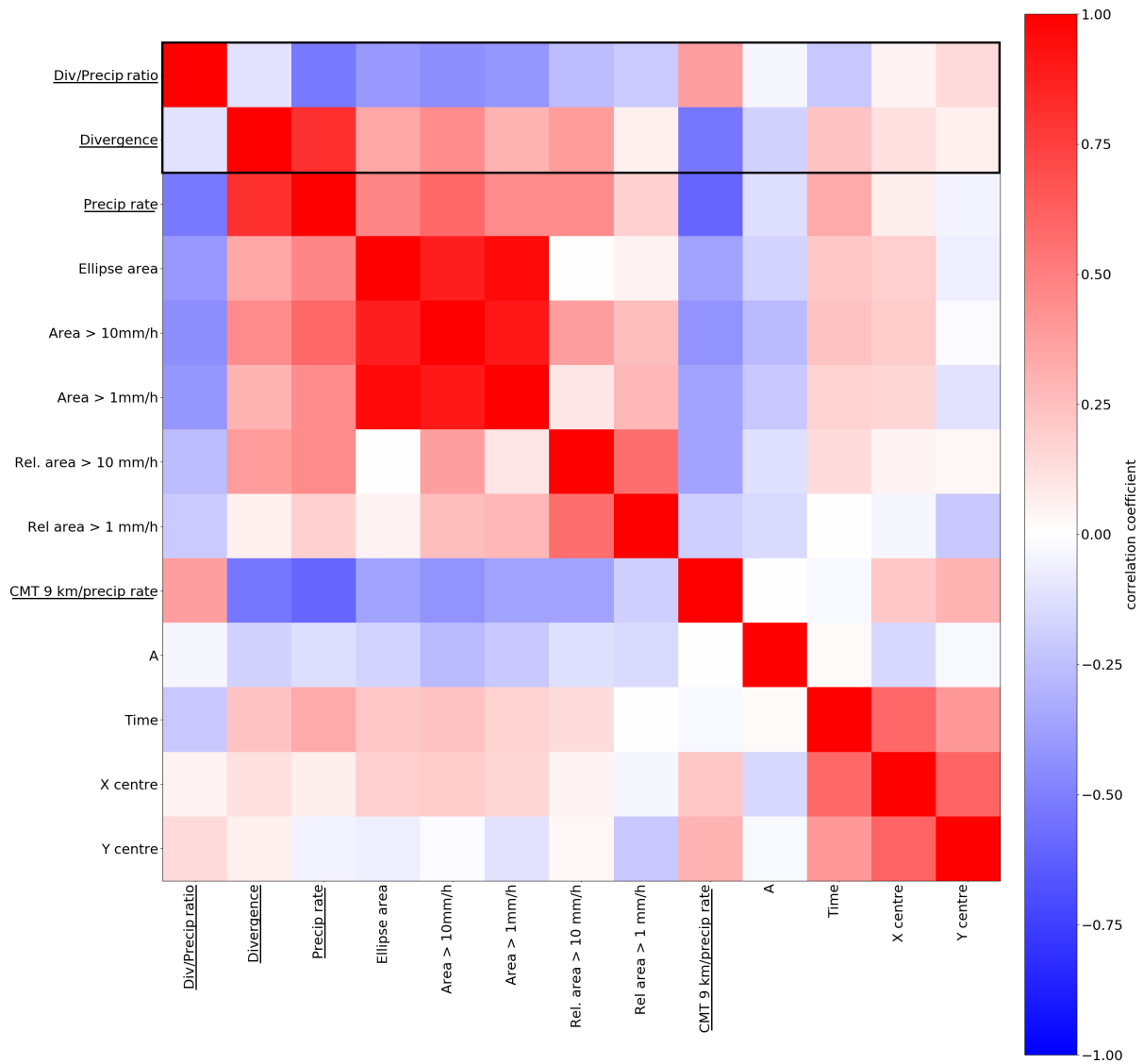


Figure 11. Overview of the correlation structures assessed in Section 6. Underlined variables indicate those that have been derived from the box integration, those without the line indicate variables extracted from ellipse parameters. Based on larger dataset with $n = 866$ samples.

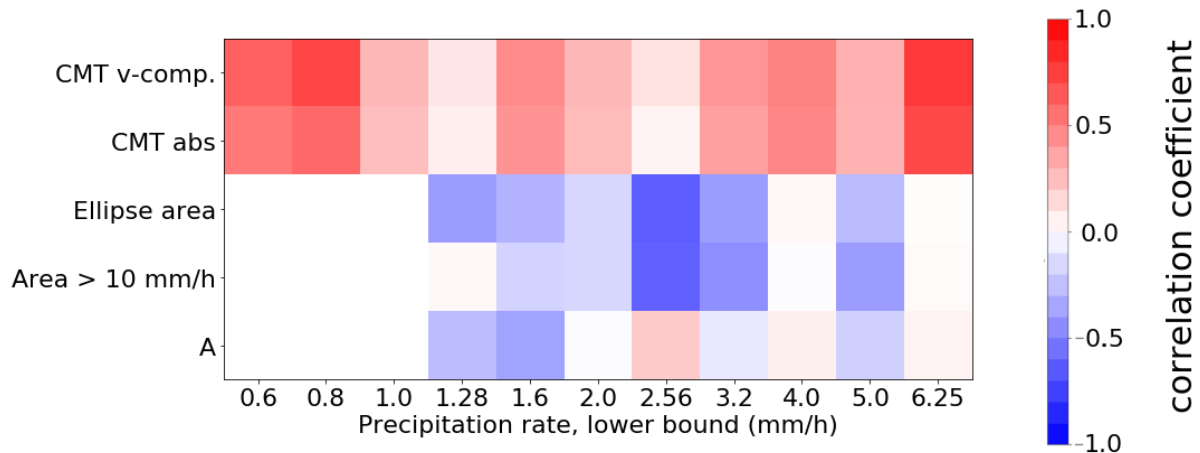


Figure 12. Overview of the correlation structures conditional on precipitation rate as assessed in Section 6. Based on the smaller dataset with $n = 456$ samples. Low precipitation signals are partially omitted due to small sample sizes and weak convection (under 1 mm/h mean precipitation rate over integration box).

705 ~~divergence accompanied by significant~~ between these two quantities is found, accompanied by substantial scatter away from
the mean relationship ~~is found. Even if the precipitation climatology is well represented, the systematic differences between~~
~~ICON-PAR and ICON-PER implies that the feedback from deep convection to its surroundings at larger scales is likely not~~
~~accurately represented by parameterised deep convection. The convective flow feedback to larger scales is likely on average~~
~~overestimated in PAR and using PER ($dx = 1$ km), the representation of outflow variability is improved. An on average~~
710 ~~overestimated deep convective outflow feedback at given global average precipitation rates may substantially impact regional~~
~~circulation in weather and climate models. It may contribute to their regional circulation biases.~~

The convection-permitting simulations have been utilised to explore hypotheses on the controlling factors in the relationship
between convective latent heating / surface precipitation and upper-level divergence derived from idealised studies (Groot and
Tost, 2023b) ~~on in a real-case simulation: In particular, we investigated~~ the impact of convective organisation ~~and aggregation~~
715 ~~as well as~~, clustering and convective momentum transport ~~on upper-tropospheric divergence in real-case simulations. The~~
~~first~~. The expected impact of convective clustering and organisation on the divergent outflows is illustrated in Figure 1: A
point source of heating and a linear heat source in the horizontal plane can be viewed as conceptual extremes of convective
clustering and organisation. The outflow strength from these two scenarios strongly varies even at identical precipitation
rate (Groot and Tost, 2023b; Nicholls et al., 1991). Therefore our first hypothesis ("dimensionality hypothesis") is that with
720 increasing elongation of a convective system outflow strength decreases (at identical precipitation rate). Furthermore, clustering
of convective cells leads to collisions of upper-level outflow, which reduces the net mass divergence through convergence
and compensating vertical circulation ("convective clustering") over mesoscale regions. The second hypothesis ("clustering
hypothesis") tested in this paper is therefore that increasing convective clustering (e.g. during temporal evolution a convective
cloud field) decreases outflow strength (at identical precipitation rate). To focus on the variability of outflow strength conditional

725 on precipitation rate, we use the ratio of upper-level divergence to surface precipitation rate, D . In this work, it has been investigated whether each of these two controlling factors on area average mass divergence contribute to variability in outflow strength in the convection-permitting configuration of ICON, during a selected convective event over Germany. Mixed results are identified with respect to the first aspect: the geometric shape of the convective heat source. On the one hand, substantial spread is clearly identified in the divergent outflow intensity as a function of precipitation rate (Figure 9). Subcategories with high and low D are found to consist of statistically different cell geometries. Furthermore, contrasts between the two subsets in ellipse orientation relative to the background flow are consistent with expectations. On the other hand, no clear correlation between elongation A of the cells and D is found.

730 The evidence for the "clustering hypothesis" is strong: the reduction of the ratio D , between net mass divergence and precipitation rate, with increasing area mean precipitation rate was confidently identified in the realistic convection-permitting ICON configuration. A consistent correlation signal is identified among several additional ellipse parameters (Section 6.2) and D , including total ellipse area and ellipse area fraction of convective precipitation (> 10 mm/h) and D . The sub-linear increase of outflow strengths with precipitation rates signifies a negative feedback from increasing diabatic heating onto upper-level divergence, as a result of outflow collisions and compensating (adjacent) convergence in the upper-troposphere. ~~states that dimensionality of the outflow (2D versus 3D and, hence, system elongation) affects the magnitude of the convective outflows.~~

740 ~~Three convective systems developing a squall-line-like structure exhibit the expected behaviour over their lifetime: as the squall-line-like structure develops and precipitation intensity increases, the mass divergence does not necessarily follow. Often, it remains in the lower half of the background distribution of conditional mass divergence. However, in the statistical analysis varied signals have been identified among the expected relations between several ellipse parameters and normalised upper-tropospheric mass divergence D . Therefore, the first hypothesis is not clearly confirmed.~~

745 ~~The second hypothesis that convective aggregation modifies the magnitude of divergent outflows, among systems with similar net latent heating rates. This hypothesis can be corroborated by our analysis of the real-case ICON-PER: correlations between outflow magnitude and convective system area and intensity are clearly negative. Furthermore, optimising outflow predictions with a power-transformed precipitation intensity confidently shows sub-linear growth, suggesting a negative feedback as a consequence of convective aggregation and organisation in the dataset. Finally, the last hypothesis about an absent impact of CMT on the outflows is rejected: conditional correlations within precipitation rate bins reveal that CMT has a small, but significant, impact on the~~ As a third and final hypothesis we investigate the direct impact of convective momentum transport on outflow strength. Given a certain precipitation rate, it has been found here that flow perturbations induced as a result of convective momentum transport have some slight impact the outflow magnitudes. mass divergence slightly in ICON-PER. However, details of the interactions cannot be derived from this study. Furthermore, note that the indirect impact

750 of convective momentum transport is technically included when convective geometry and clustering are investigated, as convective momentum transport can impact convective organisation and therefore precipitation rates (see also Groot and Tost, 2023b)

7.2 Discussion

~~The applied methods improve~~ Our analysis provides insight into the divergent outflow variability in ICON for the studied event, as hypotheses can be investigated. selected case-study and the mechanisms that can govern the variability. ~~Outflow variability will not collapse onto a linear relationship without variability due to robust effects of convective organisation that have been assessed in a multivariate way. Therefore, this study confirms the results from idealised LESsimulations (Groot and Tost, 2023b)~~ The amplitude of divergent outflow is proportional to net latent heating rates, which has been known (Nicholls et al., 1991). However, at a certain latent heating intensity, it is now also clear that LES and convection-permitting NWP allow for a substantial variation in mean divergent upper-tropospheric outflow rates (see also Groot and Tost, 2023b). Our ICON case study indicates that the variation of outflow magnitudes at a given heating rate is determined by the geometric structure of the convective systems, consistently with earlier results from LES, but along with small direct modulations by convective momentum transport in ICON-PER.

7.2.1 Dimensionality hypothesis ~~Conceptual understanding of divergent outflows~~

The dimensionality hypothesis "~~dimensionality hypothesis~~" is not strongly supported by our analysis, albeit some indirect evidence points to an impact of dimensionality on divergent outflows. Three suggestions are made, why the dimensionality hypothesis is not strongly supported by the statistics:

- The chosen metric is sub-optimal: it is not able to distinguish ~~nearly-2D and nearly-3D convection well~~ ~~nearly-two-dimensional ("line source of heating") and nearly-three-dimensional convection ("point source") well~~ (Figure 1); furthermore, real cases often cannot be unambiguously ~~categorized~~ ~~categorised~~ into the two classes (Trier et al., 1997) (e.g. Trier et al., 1997).
- The (elevated) shear profile of this case does not induce ~~sufficient variability~~ ~~the maximum possible variation~~ in dimensionality of the deep ~~convection~~ ~~convective overturning~~ (from nearly-two-dimensional to nearly-three-dimensional).
- Opposing statistical ~~patterns~~ ~~relations between ellipse parameter estimates (e.g. ellipse elongation A) and the potential effect on mass divergence~~ compensate each other, even within precipitation bins.

Each of these will be discussed in the following paragraphs one by one. ~~Consequently, the outflow dimensionality seems to contribute only weakly to outflow variability, while the effect of organisation and aggregation is strongly present. Nevertheless, the signal associated with squall line development supports the dimensionality argument, consistently with Bretherton and Smolarkiewicz (2002) and others.~~

The first possibility is that our metric for system dimensionality, namely the ellipse elongation, ~~is not fully adequate, in particular since many convective system in ICON-PER are relatively small. Only few does not adequately map the variability in geometry of small convective systems. In our case study only few systems~~ develop clear structures. ~~A solution is to investigate if a poor metric buries the signal by applying the method to a larger set of "PER"-like simulations of various cases. Another solution would be investigating~~ Future assessments involving more extensive datasets of convection-permitting simulations

from across the globe and various cases would clear-up on this issue. Another option would be to investigate if other algorithms, using e.g. a storm-relative flow analysis, could assist the dimensionality-geometric analysis of a wide-wider mixture of organised systems. That may be combined with our method and is achievable (Groot and Tost, 2023b; Trier et al., 1997). Earlier studies, e.g., by Groot and Tost (2023b) and Trier et al. (1997), could be a useful guideline for such follow-up investigations.

795 Furthermore, the second possibility is that the shear profiles of Groot and Tost (2023b) impose a clearer separation between 2D and 3D outflow regimes than in our event here. A profile with stronger low-level shear (0-3 km) would enhance squall line formation and initiate corresponding convection resembling the 2D regime closer. It is worthwhile to revisit the dimensionality hypothesis with a larger ensemble of convective systems including cases of well-developed squall lines and a (sub-)ensemble of less strongly organised convection. The development phase of squall lines could be particularly interesting. A second

800 explanation of improper sorting of overturning characteristics could be insufficient variability in the overturning dimensionality in the investigated case-study. We essentially may not sample nearly-two-dimensional convective overturning, which is found in well-organised squall lines (e.g. Moncrieff, 1992; Trier et al., 1997; Groot and Tost, 2023b). These include a convergence line near the surface with strong updrafts along a concentrated line, where a strong density current moves at about the speed of the convective cells. For such well-organised squall lines, we would expect strong similarities in orientations of detected ellipses as

805 well as very elongated ellipses. We found such a pattern, but squall line segments have lengths of only up to about 100 km. Long and narrow squall lines forming in very strong near-surface shear (like in Groot and Tost (2023a); Rotunno et al. (1988); Coniglio et al. (2000)) probably resemble two-dimensional convective overturning much better than systems sampled in our case-study. Well-organised squall-lines are typically associated with strong shear at low levels perpendicular to the orientation of the convergence line (also associated with a strong cold pool). This causes the described geometric characteristics and the convective overturn to be

810 quasi-2D. However, in our case strong wind shear is concentrated in a somewhat elevated layer (in PER: at 2-4 km a.g.l.) and is not nearly perpendicular to the frontal boundary (Section 2). Therefore convective overturning may more closely resemble three-dimensional overturning than two-dimensional convective overturning even for the most strongly organised near-frontal convective systems.

Lastly, because of compensating anti-correlation between estimated ellipse elongation parameter A and convective aggregation

815 tion may very well be anti-correlated. However, based on our conceptual understanding both can plausibly impact the mass divergence. Therefore, their effects on the mass divergence could potentially compensate each other (see Figure 11). Therefore, a third possibility is that axis ratio for the weak evidence obtained for the "dimensionality hypothesis" is that ellipse parameter A hides the direct dimensionality signal in the outflow variability. The signal may even be hidden if conditional correlations between A and D within precipitation rate bins are considered (Figure 12). This is possible if A is a sub-optimal proxy for the

820 dimensionality of convective outflows. Two correlation effects within precipitation bins. The two correlation effects expected (based on conceptual understanding) could oppose another, namely convective aggregation and A as a proxy for outflow dimensionality, within precipitation bins. Only with the number of precipitation bins approaching infinity (i.e. infinitely narrow bins), the two opposing effects can be truly filtered out and circumvented; so a much larger dataset would strongly reduce the effect (which would require some adjustments in the methods). Consequently, analysed patterns may seemingly be explained

825 by aggregation-convective clustering only, even if the dimensionality hypothesis explains a substantial proportion of the exam-

ined outflow variability.

~~Summarised, the outflow geometry and dimensionality of convective overturn seems to contribute only weakly to outflow variability. Still, the signal associated with squall line development supports the dimensionality argument, consistently with findings by Bretherton and Smolarkiewicz (1989); Nicholls et al. (1991); Groot and Tost (2023b) and others.~~

830 Nevertheless, if the dimensionality and aggregation hypotheses are strongly interrelated, as suggested in Groot and Tost (2023b), it would be surprising if ~~a compensation between the correlation signals would occur. The dimensionality hypothesis should probably be easier~~ the effect of dimensionality is harder to prove than the aggregation hypothesis. Therefore, a follow-up study with a ~~squall line ensemble versus less strongly organised deep convection~~ wider variety of convective cloud field structures and degrees of clustering/organisation (including some strongly organised squall lines) is needed to resolve this
835 ~~possible paradox issue.~~

7.2.2 CMT hypothesis

The impact of CMT on the ~~outflows~~ outflow strength is found to be much more pronounced here than in the LES study of Groot and Tost (2023b). ~~CMT was not found to (directly) affect the convective outflows in the LES-simulations, possibly because the imposed shear layer was too shallow. This may be due to the difference in the wind shear profiles between the LES study and~~
840 ~~the real case investigated here:~~ Upper-tropospheric wind shear was completely absent in ~~that configuration~~ (the initial conditions of) the LES-configuration, whereas any real world has non-zero shear in the upper troposphere. ~~In the LES-simulations, the shallow shear configuration was used to reduce cell propagation through the small domain.~~ Shallow shear configurations (e.g. all shear at levels below 3 km altitude) can reduce the average height that parcels in convective cells reach (Coniglio et al., 2006) ~~and the~~. ~~The~~ associated reduced vertical overturning ~~suppresses~~ would subsequently suppress the interaction between
845 the shear layer and the divergent outflows (in agreement with Brown (1999)), ~~such that eddy momentum transport through the upper half of the troposphere may hardly occur.~~ Therefore, ~~the effective local acceleration or deceleration of the flow might not reach the upper-troposphere. Hence, the~~ impact of CMT on the ~~outflows~~ outflow strength is likely suppressed in Groot and Tost (2023b) ~~and CMT was not found to (directly) affect the convective outflows in the LES-simulations. A comparison of LES-simulations where the shear is more evenly distributed over a deeper layer, with a setup similar to (Groot and Tost, 2023b)~~
850 ~~, would be beneficial to assess if this hypothesis is true. The presence of shear over a much deeper layer is a more realistic scenario and therefore should be assessed in a complementary study with LES-configuration.~~

Additionally, the ICON-PER configuration is arguably most suitable for detecting subtle (reasonable, real case) CMT impacts on the divergent outflows. Conversely, the setup does not allow in-depth understanding of the mechanisms behind outflow variability, due to the complexity of the scenario and the amplitude of the systems in close spatio-temporal proximity. ~~Additional~~
855 ~~LES-experiments targeting CMT could enhance insight in future studies.~~

7.2.3 Further research

~~To summarise, this study shows further investigation is needed to thoroughly understand the role of dimensionality for the magnitude of divergent outflows in a practical NWP-setting. Furthermore, convective organisation and aggregation are found~~

to be key players for the magnitude of divergent outflows in practice, which is only accounted for by convection-permitting simulations at 1 km horizontal grid spacing.

7.3 Implications

Overall, it is clear that further research is needed for a basic understanding of the interaction between the characteristics of divergent convective outflows and their relation to convective momentum transport, as well as to further describe the two-fold (direct and indirect) role of convective clustering and organisation therein. The different role of CMT for upper-level divergence between the LES and NWP study provide little foundation for more than speculation of the mechanisms that may act. Similarly, to investigate how the CMT-accelerations could mechanistically affect flow predictability is beyond the scope of this work and would require advanced, specifically tailored methods.

7.3 Implications for predictability in NWP

7.3.1 Predictability and uncertainty in divergent convective outflow strength

Previous studies investigating the predictability of the atmosphere from a dynamical perspective have identified that ensemble spread amplifies strongly in regions of precipitation, and in particular convection (e.g. Zhang, 2005; Zhang et al., 2007; Selz and Craig, 2019). Baumgart et al. (2019) have investigated the sequence of dynamical processes that (on average) contribute to mid-latitude growth of flow perturbations. They proposed that latent heating tendencies from their deep convection scheme in ICON may induce differential divergent winds in the upper troposphere, which may interact with a nearby jet stream to constructively amplify perturbation growth. Subsequently, further non-linear growth of flow perturbations in the upper troposphere is driven by differential advection. Practical cases where precipitation systems importantly reduce atmospheric predictability are nevertheless thought to be rare, at typical state-of-the-art initial state uncertainty amplitudes (see Lorenz, 1969; Rodwell et al., 2013; Durran and Gingric

An open key question is whether the variability in flow perturbations associated with convective outflows in the upper troposphere is comparably (and reliably) represented in simulations with resolved and parameterised deep convection. The findings of this work suggest that this is only the case when deep convection is explicitly resolved. In parameterised setup, our results suggest that the ensemble is underdispersive in terms of outflow variability with a strong linear correlation between divergent outflow and precipitation rate variability.

This work once more confirms the strong link between precipitation variability and flow variability in an ensemble. This close connection may lead to perturbation growth in a forecast or spread in an ensemble. The downstream propagation of perturbations is not directly addressed here. Nevertheless, the spatial-temporal distribution of divergence variability (Figure 7) suggests is consistent with a potential role for divergent outflows propagating precipitation variability and other convective variability (e.g. mostly: CMT) to large-scale dynamics. The potential downstream impact of convective variability via this (and other) mechanisms is addressed by e.g., Baumgart et al. (2019) and Rodwell et al. (2013). Furthermore, this uncertainty in dynamics at large scales, in line with Baumgart et al. (2019).

7.3.2 Splitting flow variability associated with convection into two components

This work suggests that the convective contribution to flow variability can be separated into a component of precipitation variability (i.e. along the x-axis of Figure 8) and another component of superposed conditional divergence variability (D variability), induced by convective organisation and aggregation. This role of convective organisation may relate to the results of Rodwell et al. (2013). Despite, a separate examination in an event with upscale impact of the convection is needed to assess the mechanisms acting.

The separation of divergence variability into the above mentioned components has significance for weather and climate modelling. Only the former component can be modelled with regular deep convection parameterisation schemes. The latter component is (nearly) absent in parameterised configurations, but is accounted for in a convection-permitting setup. Assessing ~~convective variability, conditioning deep convective variability~~ deep convective variability, conditioned on precipitation rate, is an important tool to illustrate the two components of variability. Thereby, the feedback between deep convection and its environment ~~is~~, for instance, can be better discerned. Common variability associated with both precipitation rate and upper-tropospheric dynamics within convective systems has been discussed in Groot and Tost (2023a, b).

7.3.3 Model representations of deep convection

Groot and Tost (2023b) shows that collisions of divergent outflows cause sub-linear increases of divergent outflow with increasing precipitation intensities, in LES. Here, we investigate the presence of this effect in two ICON configurations, and find it only in convection-permitting ICON. At low precipitation rates, the ratio between mass divergence and precipitation rate in ICON-PAR overlaps with the upper range of the same ratio in ICON-PER and the LES configuration of (Groot and Tost, 2023b). Nevertheless, both ICON-PER and the aforementioned LES study do not maintain these high values of D up to higher precipitation intensities: the values of D decrease at these precipitation rates.

The systematic differences between ICON-PAR and ICON-PER regarding the relation between surface precipitation and upper-level divergence (Fig. 8) suggest that the feedback from deep convection to its surroundings at larger scales is likely not accurately represented with parameterised deep convection, even if the precipitation climatology is well represented: parameterised ensembles seem to be underdispersive in terms of corresponding dynamical variability at a given precipitation rate (Figure 8). Furthermore, the convective flow feedback to larger scales is likely on average overestimated in PAR. An on average overestimated deep convective outflow feedback at given global average precipitation rates may substantially impact regional circulation patterns in weather and climate models, potentially contributing to subsequent regional circulation biases. It is known that models represent convective organisation imperfectly, especially whenever a parameterisation scheme is used. Our work suggests that it is important to increase the understanding of convective organisation biases in models. These biases may interact with biases in the precipitation climatology, and even cause compensating errors in NWP. However, these compensating errors may be hidden, unless mesoscale mass divergence spread produced at given precipitation rates is specifically included in an analysis. Apart from conditioning on precipitation rates, conditioning on e.g., the diurnal cycle and regional convective characteristics can importantly contribute to improved simulations across resolutions (e.g. Bechtold et al., 2014; Becker

925 . Convective organisation biases are known to affect squall line representation in convection-permitting models (Becker et al., 2021)
and could likely contaminate succinct results in ICON setups like ours. The conceptual model of (Groot and Tost, 2023b),
verified against ICON in this work, provides a possible pathway of how grid scale storms could introduce mesoscale circulation
biases despite an accurate precipitation climatology.

930 Upscale growth and clustering of convective systems are found to be key players for the magnitude of divergent outflows in
practice, which is properly accounted for only by convection-permitting simulations at about 1 km horizontal grid spacing.
This is probably because the small-scale gravity waves emitted by individual deep convective elements, and their interactions
after collisions, are only well-resolved at this grid spacing. Based on the second and to a lesser extent third hypothesis of this
work, convective ~~organisation and aggregation affect dynamics.~~ clustering affects dynamics. Divergent winds associated with
convective heating increase non-linearly with the heating rate as convective systems grow. Therefore, it is needed to include
~~these factors~~ non-linear increments of divergence with increasing intensity of convective systems into error growth studies,
935 assisting ~~them~~ these studies to extend all the way from the convective to the planetary scales. Consequently, the conditional
convective perspective shaped here can be connected with the Baumgart et al. (2019)-perspective.

8 Conclusions

The multivariate exploration of divergent ~~outflows~~ outflow strength of deep moist convection in real case weather prediction
shows that their ~~dependency is~~ controlling processes are rather complex and cannot easily be distinguished and assigned to
940 individual ~~processes~~ mechanisms. However, based on the analysis of a single convective event, major variability of the rela-
tionship ~~of precipitation~~ between precipitation rate and upper-tropospheric divergent outflow is explained by effects that were
also present in LES-analyses (Groot and Tost, 2023b). The following can be concluded on variability in upper-tropospheric
divergent outflows from deep convection (~~"this outflow"~~ as to this case study):

- 945 – The outflow is responsible for major ensemble spread in the divergent part of the upper-tropospheric wind during a
convective event.
- Convection-permitting (1 km horizontal grid spacing) simulations represent the effect of aggregation on divergent out-
flow from deep convection and ~~an envelope~~ substantial spread of divergent outflow exists at a given net latent heating
rate.
- Using simulations at coarser resolution probably implies assuming a (near-)linear relationship between the outflow and
950 net latent heating.
- ~~Indications exist showing~~ Various indications show that the fingerprint of dimensionality is represented in variability of
~~this outflow~~ convective outflow strength in ICON convection-permitting settings, but a case study comparing squall lines
that highly resemble 2D-convection with less organised convection is needed to increase the confidence in this finding.
- Convective momentum transport seems to weakly affect this outflow strength directly.

955 – To understand convectively induced flow perturbations better, a separation into two components of convective variability is necessary: 1. variability in predicted mesoscale precipitation rates; 2. representation of the residual (conditional) flow perturbations, which depend on the cloud-scale dynamics.

960 The results of this work strongly suggest that the interactions between gravity waves emitted by heating of individual clouds is likely of prime importance for the representation of divergent outflows from organised convection, which can successful be achieved at convection-permitting resolution. Additional case studies are needed to revisit the role of the dimensionality of convective overturning.

Code and data availability. The code used in this work and the output for one PER and one PAR simulation are available in Groot and Kuntze (2023) (last accessed: 16-02-2023).

Appendix A: Table of parameters in ellipse dataset

Table A1. List of parameters in the dataset of ellipse records, with their descriptions.

Name of parameter	Unit	Explanation (if necessary)	Symbol
Ellipse id	#	Each ellipse comes with an id	
Time stamp	# 5 min	Each corresponding output time step has a time stamp	
Axis ratio	-	Ratio between major and minor axis of ellipse	A
Mean precipitation rate	mm/h	Mean surface precipitation rate over convective system's track following box	
Mean mass divergence	$\frac{kg}{m^3 s}$	Mean upper tropospheric (380-180 hPa) mass divergence rate over convective system's track following box	
Div/precip ratio	$\frac{kg \cdot mm}{m^3 s^1 h^1}$	Ratio between box mean mass divergence and box mean precipitation rate	D
U-component of CMT eddy flux	$m^2 s^{-2}$	Mean value of $u'w'$ at model level 25, about 315 hPa, where ' indicates domain average relative velocity perturbations	
V-component of CMT eddy flux	$m^2 s^{-2}$	Mean value of $v'w'$ at model level 25, about 315 hPa	
Absolute vertical integral of CMT acceleration	$m^2 s^{-2}$	Mean value of $[(u'w')^2 + (v'w')^2]^{\frac{1}{2}}$ at model level 25, about 315 hPa	
Ratio absolute integral of CMT acceleration over precip rate	$\frac{m^2 h}{s^2 mm^1}$	As above, but relative to precipitation rate in mm/h (also computed for U and V component separately)	C
Xcentre	grid cell #	Centre of the fitted ellipse in zonal direction	
Ycentre	grid cell #	Centre of the fitted ellipse in meridional direction	
Ellipse angle/orientation	°	Orientation of the major axis of the ellipse with respect to a reference direction	O
Major axis length	km		
Minor axis length	km		
Ellipse area	# grid cell ²	Area of the ellipse that has been fit, can be converted to square km (1 grid cell is approximately 4 km ²)	
Mean precipitation rate over ellipse	mm/h	Mean precipitation rate over ellipse only	
Area >10 mm/h precipitation rate	-	Fraction of ellipse exceeding 10 mm/h ("convective") precipitation	
Area >1 mm/h precipitation rate	-	Fraction of ellipse exceeding 1 mm/h ("stratiform + convective") precipitation	
X distance ellipse and box centre	km	Distance between box centre and fitted ellipse in x-direction	
Y distance ellipse and box centre	km	Distance between box centre and fitted ellipse in y-direction	
Total distance ellipse/box	km	Total distance obtained from its x- and y-component	

Table B1. [Ellipse parameters associated with two subsets of the full dataset analyzed in Section 6.1 are sorted separately in the below table.](#)

Parameter	Full dataset	Subset low D	Subset high D
A_{mean} (-)	0.56	0.54	0.60
$O_{st.dev.}$ ($^{\circ}$)	44	32	45

Author contributions. EG (ICON-PAR) and PK (ICON-PER) carried out the simulations for this work, under the supervision of HT and AM. EG designed the study, developed the ellipse fitting algorithm, carried out the analysis and wrote the manuscript with contributions from all co-authors.

Competing interests. The authors have no competing interests to declare.

970 *Acknowledgements.* The research leading to these results has been done within the subprojects ‘A1 - Multiscale analysis of the evolution of forecast uncertainty’ and ‘B1 - Microphysical uncertainties in hailstorms using statistical emulation and stochastic cloud physics’ of the Transregional Collaborative Research Center SFB / TRR 165 ‘Waves to Weather’ funded by the German Research Foundation (DFG). The authors would also like to acknowledge the computing time granted on the supercomputer MOGON 2 at Johannes Gutenberg-University Mainz (hpc.uni-mainz.de, last accessed: 02-02-2023).

- Adams-Selin, R. D.: Impact of Convectively Generated Low-Frequency Gravity Waves on Evolution of Mesoscale Convective Systems, *Journal of the Atmospheric Sciences*, 77, 3441 – 3460, <https://doi.org/10.1175/JAS-D-19-0250.1>, 2020a.
- Adams-Selin, R. D.: Sensitivity of MCS Low-Frequency Gravity Waves to Microphysical Variations, *Journal of the Atmospheric Sciences*, 77, 3461 – 3477, <https://doi.org/10.1175/JAS-D-19-0347.1>, 2020b.
- 980 Arakawa, A.: The Cumulus Parameterization Problem: Past, Present, and Future, *JOURNAL OF CLIMATE*, 17, 2493–2525, 2004.
- Baumgart, M., Ghinassi, P., Wirth, V., Selz, T., Craig, G. C., and Riemer, M.: Quantitative View on the Processes Governing the Upscale Error Growth up to the Planetary Scale Using a Stochastic Convection Scheme, *Monthly Weather Review*, 147, 1713–1731, <https://doi.org/10.1175/mwr-d-18-0292.1>, 2019.
- Bechtold, P., Semane, N., Lopez, P., Chaboureaud, J., Beljaars, A., and Bormann, N.: Representing equilibrium and nonequilibrium convection
985 in large-scale models, *Journal of the Atmospheric Sciences*, 71, 734–753, 2014.
- Becker, T., Bechtold, P., and Sandu, I.: Characteristics of convective precipitation over tropical Africa in storm-resolving global simulations, *Quarterly Journal of the Royal Meteorological Society*, 147, 4388–4407, <https://doi.org/https://doi.org/10.1002/qj.4185>, 2021.
- Bierdel, L., Selz, T., and Craig, G.: Theoretical aspects of upscale error growth through the mesoscales: an analytical model, *Quarterly Journal of the Royal Meteorological Society*, 143, 3048–3059, <https://doi.org/10.1002/qj.3160>, 2017.
- 990 Bierdel, L., Selz, T., and Craig, G. C.: Theoretical aspects of upscale error growth on the mesoscales: Idealized numerical simulations, *Quarterly Journal of the Royal Meteorological Society*, 144, 682–694, <https://doi.org/10.1002/qj.3236>, 2018.
- Bretherton, C. S. and Smolarkiewicz, P. K.: Gravity Waves, Compensating Subsidence and Detrainment around Cumulus Clouds, *Journal of Atmospheric Sciences*, 46, 740 – 759, [https://doi.org/10.1175/1520-0469\(1989\)046<0740:GWCSAD>2.0.CO;2](https://doi.org/10.1175/1520-0469(1989)046<0740:GWCSAD>2.0.CO;2), 1989.
- Brown, A.: Large-eddy simulation and parametrization of the effects of shear on shallow cumulus convection, *Boundary-layer meteorology*,
995 91, 65–80, 1999.
- Clarke, S., Gray, S., and Roberts, N.: Downstream influence of mesoscale convective systems. Part 1: influence on forecast evolution, *Quarterly Journal of the Royal Meteorological Society*, 145, 2933–2952, <https://doi.org/https://doi.org/10.1002/qj.3593>, 2019a.
- Clarke, S., Gray, S., and Roberts, N.: Downstream influence of mesoscale convective systems. Part 2: Influence on ensemble forecast skill and spread, *Quarterly Journal of the Royal Meteorological Society*, 145, 2953–2972, <https://doi.org/https://doi.org/10.1002/qj.3613>, 2019b.
- 1000 Coniglio, M. C., Stensrud, D. J., and Wicker, L. J.: Effects of upper-level shear on the structure and maintenance of strong quasi-linear mesoscale convective systems, *Journal of the Atmospheric Sciences*, 63, 1231–1252, <https://doi.org/10.1175/jas3681.1>, 2006.
- Done, J. M., Craig, G. C., Gray, S. L., Clark, P. A., and Gray, M. E. B.: Mesoscale simulations of organized convection: Importance of convective equilibrium, *Quarterly Journal of the Royal Meteorological Society*, 132, 737–756, <https://doi.org/https://doi.org/10.1256/qj.04.84>, 2006.
- 1005 Durran, D. and Gingrich, M.: Atmospheric Predictability: Why Butterflies Are Not of Practical Importance, *Journal of the Atmospheric Sciences*, 71, 2476 – 2488, <https://doi.org/10.1175/JAS-D-14-0007.1>, 2014.
- Giorgetta, M., Brokopf, R., Cruieger, T., Esch, M., Fiedler, S., Helmert, J., Hohenegger, C., Kornblueh, L., Köhler, M., Manzini, E., et al.: ICON-A, the atmosphere component of the ICON earth system model: I. Model description, *Journal of Advances in Modeling Earth Systems*, 10, 1613–1637, 2018.
- 1010 Grant, L. D., P., L. T., and van den Heever, S. C.: The role of cold pools in tropical oceanic convective systems, *Journal of the atmospheric sciences*, 75, 2615–2634, <https://doi.org/10.1175/jas-d-17-0352.1>, 2018.

- Grant, L. D., Moncrieff, M. W., Lane, T. P., and van den Heever, S. C.: Shear-parallel tropical convective systems: Importance of cold pools and wind shear, *Geophysical Research Letters*, 47, e2020GL087720, 2020.
- Groot, E.: An analysis of variability and predictability of organised deep convection and its divergent upper tropospheric outflow, 2023.
- 1015 Groot, E. and Kuntze, P.: Dataset of "Divergent convective outflow in ICON deep convection permitting and parameterised deep convection simulations": sample simulations and the tool "EFiDaGe for CoSy", <https://doi.org/10.5281/zenodo.7541630>, Funded by TRR-165 (DFG): 'Wavestoweather' (see wavestoweather.de), 2023.
- Groot, E. and Tost, H.: Evolution of squall line variability and error growth in an ensemble of large eddy simulations, *Atmospheric Chemistry and Physics*, 23, 565–585, <https://doi.org/10.5194/acp-23-565-2023>, 2023a.
- 1020 Groot, E. and Tost, H.: Divergent convective outflow in large-eddy simulations, *Atmospheric Chemistry and Physics*, 23, 6065–6081, <https://doi.org/10.5194/acp-23-6065-2023>, 2023b.
- Houze, R. A.: Mesoscale convective systems, *Reviews of Geophysics*, 42, <https://doi.org/10.1029/2004rg000150>, 2004.
- Houze, R. A.: 100 Years of Research on Mesoscale Convective Systems, *Meteorological Monographs*, 59, 17.1 – 17.54, <https://doi.org/10.1175/AMSMONOGRAPHS-D-18-0001.1>, 2018.
- 1025 Judt, F.: Atmospheric Predictability of the Tropics, Middle Latitudes, and Polar Regions Explored through Global Storm-Resolving Simulations, *Journal of the Atmospheric Sciences*, 77, 257 – 276, <https://doi.org/10.1175/JAS-D-19-0116.1>, 2020.
- Keane, R. J., Craig, G., Keil, C., and Zängl, G.: The Plant–Craig Stochastic Convection Scheme in ICON and Its Scale Adaptivity, *Journal of the Atmospheric Sciences*, 71, 3404–3415, <https://journals.ametsoc.org/doi/abs/10.1175/JAS-D-13-0331.1>, 2014.
- Lane, T. P. and Reeder, M. J.: Convectively Generated Gravity Waves and Their Effect on the Cloud Environment, *Journal of the Atmospheric Sciences*, 58, 2427 – 2440, [https://doi.org/10.1175/1520-0469\(2001\)058<2427:CGGWAT>2.0.CO;2](https://doi.org/10.1175/1520-0469(2001)058<2427:CGGWAT>2.0.CO;2), 2001.
- 1030 Lawrence, M. and Salzmann, M.: On interpreting studies of tracer transport by deep cumulus convection and its effects on atmospheric chemistry, *Atmospheric Chemistry and Physics*, 8, 6037–6050, 2008.
- Lorenz, E.: The predictability of a flow which possesses many scales of motion, *Tellus*, 21, 289–307, <https://doi.org/10.3402/tellusa.v21i3.10086>, 1969.
- 1035 Mapes, B. E.: Gregarious Tropical Convection, *Journal of Atmospheric Sciences*, 50, 2026 – 2037, [https://doi.org/10.1175/1520-0469\(1993\)050<2026:GTC>2.0.CO;2](https://doi.org/10.1175/1520-0469(1993)050<2026:GTC>2.0.CO;2), 1993.
- Mapes, B. E. and Houze, R. A.: Diabatic Divergence Profiles in Western Pacific Mesoscale Convective Systems, *Journal of Atmospheric Sciences*, 52, 1807 – 1828, [https://doi.org/10.1175/1520-0469\(1995\)052<1807:DDPIWP>2.0.CO;2](https://doi.org/10.1175/1520-0469(1995)052<1807:DDPIWP>2.0.CO;2), 1995.
- Matsunobu, T., Keil, C., and Barthlott, C.: The impact of microphysical uncertainty conditional on initial and boundary condition uncertainty under varying synoptic control, *Weather and Climate Dynamics*, 3, 1273–1289, <https://doi.org/10.5194/wcd-3-1273-2022>, 2022.
- 1040 Moncrieff, M. W.: Organized Convective Systems: Archetypal Dynamical Models, Mass and Momentum Flux Theory, and Parametrization, *Quarterly Journal of the Royal Meteorological Society*, 118, 819–850, <https://doi.org/10.1002/qj.49711850703>, 1992.
- Morrison, H.: Impacts of Updraft Size and Dimensionality on the Perturbation Pressure and Vertical Velocity in Cumulus Convection. Part I: Simple, Generalized Analytic Solutions, *Journal of the Atmospheric Sciences*, 73, 1441 – 1454, <https://doi.org/10.1175/JAS-D-15-0040.1>, 2016a.
- 1045 Morrison, H.: Impacts of Updraft Size and Dimensionality on the Perturbation Pressure and Vertical Velocity in Cumulus Convection. Part II: Comparison of Theoretical and Numerical Solutions and Fully Dynamical Simulations, *Journal of the Atmospheric Sciences*, 73, 1455 – 1480, <https://doi.org/10.1175/JAS-D-15-0041.1>, 2016b.

- Muller, C., Yang, D., Craig, G., Cronin, T., Fildier, B., Haerter, J., Hohenegger, C., Mapes, B., Randall, D., Shamekh, S., and Sherwood, S.: Spontaneous Aggregation of Convective Storms, *Annual Review of Fluid Mechanics*, 54, 133–157, <https://doi.org/10.1146/annurev-fluid-022421-011319>, 2022.
- Nicholls, M. E., Pielke, R. A., and Cotton, W. R.: Thermally Forced Gravity Waves in an Atmosphere at Rest, *Journal of Atmospheric Sciences*, 48, 1869 – 1884, [https://doi.org/10.1175/1520-0469\(1991\)048<1869:TFGWIA>2.0.CO;2](https://doi.org/10.1175/1520-0469(1991)048<1869:TFGWIA>2.0.CO;2), 1991.
- Ollinaho, P., Lock, S., Leutbecher, M., Bechtold, P., Beljaars, A., Bozzo, A., Forbes, R., Haiden, T., Hogan, R., and Sandu, I.: Towards process-level representation of model uncertainties: stochastically perturbed parametrizations in the ECMWF ensemble, *Quarterly Journal of the Royal Meteorological Society*, 143, 408–422, 2017.
- OpenCV: Open Source Computer Vision Library, utilized in 2022.
- Palmer, T.: Stochastic weather and climate models, *Nature Reviews Physics*, 1, 463–471, 2019.
- Pandya, R., Durran, D., and Bretherton, C.: Comments on "Thermally Forced Gravity Waves in an Atmosphere at Rest", *Journal of the atmospheric sciences*, 50, 4097–4101, <ftp://eos.atmos.washington.edu/pub/breth/papers/1993/pandya-etal.pdf>, 1993.
- Pandya, R. E. and Durran, D. R.: The influence of convectively generated thermal forcing on the mesoscale circulation around squall lines, *Journal of the Atmospheric Sciences*, 53, 2924–2951, [https://doi.org/10.1175/1520-0469\(1996\)053lt;2924:tiocgtgt;2.0.co;2](https://doi.org/10.1175/1520-0469(1996)053lt;2924:tiocgtgt;2.0.co;2), 1996.
- Prill, F., Reinert, D., Rieger, D., and Zängl, G.: ICON Model Tutorial 2020, Available at https://www.dwd.de/DE/leistungen/nwv_icon_tutorial/pdf_einzelbaende/icon_tutorial2020.pdf, 2020.
- Rodwell, M. J., Magnusson, L., Bauer, P., Bechtold, P., Bonavita, M., Cardinali, C., Diamantakis, M., Earnshaw, P., Garcia-Mendez, A., Isaksen, L., Källén, E., Klocke, D., Lopez, P., McNally, T., Persson, A., Prates, F., and Wedi, N.: Characteristics of Occasional Poor Medium-Range Weather Forecasts for Europe, *Bulletin of the American Meteorological Society*, 94, 1393–1405, <https://doi.org/10.1175/bams-d-12-00099.1>, 2013.
- Rotunno, R., Klemp, J. B., and Weisman, M. L.: A theory for strong, long-lived squall lines, *Journal of the Atmospheric Sciences*, 45, 463–485, [https://doi.org/10.1175/1520-0469\(1988\)045lt;0463:atfslgt;2.0.co;2](https://doi.org/10.1175/1520-0469(1988)045lt;0463:atfslgt;2.0.co;2), 1988.
- Satoh, M., Stevens, B., Judt, F., Khairoutdinov, M., Lin, S., Putman, W., and Düben, P.: Global cloud-resolving models, *Current Climate Change Reports*, 5, 172–184, 2019.
- Schumacher, C., Houze, R. A., and Kraucunas, I.: The Tropical Dynamical Response to Latent Heating Estimates Derived from the TRMM Precipitation Radar, *Journal of the Atmospheric Sciences*, 61, 1341 – 1358, [https://doi.org/10.1175/1520-0469\(2004\)061<1341:TTDRTL>2.0.CO;2](https://doi.org/10.1175/1520-0469(2004)061<1341:TTDRTL>2.0.CO;2), 2004.
- Seifert, A.: A revised cloud microphysical parameterization for COSMO-LME, *COSMO Newsletter*, 7, 25–28, 2008.
- Seifert, A. and Beheng, K.: A two-moment cloud microphysics parameterization for mixed-phase clouds. Part 1: Model description, *Meteorology and atmospheric physics*, 92, 45–66, 2006.
- Selz, T. and Craig, G. C.: Upscale Error Growth in a High-Resolution Simulation of a Summertime Weather Event over Europe, *Monthly Weather Review*, 143, 813–827, <https://doi.org/10.1175/mwr-d-14-00140.1>, 2015a.
- Selz, T. and Craig, G. C.: Simulation of upscale error growth with a stochastic convection scheme, *Geophysical Research Letters*, 42, 3056–3062, <https://doi.org/10.1002/2015gl063525>, 2015b.
- Selz, T., Riemer, M., and Craig, G.: The transition from practical to intrinsic predictability of midlatitude weather, *Journal of the Atmospheric Sciences*, <https://doi.org/10.1175/JAS-D-21-0271.1>, 2022.
- Stechmann, S. N. and Majda, A. J.: Gravity waves in shear and implications for organized convection, *AMETSOC*, <https://doi.org/10.1175/2009JAS2976.1>, 2009.

- Tiedtke, M.: A comprehensive mass flux scheme for cumulus parameterization in large-scale models, *Monthly weather review*, 117, 1779–1800, 1989.
- 1090 Trier, S. B., Skamarock, W. C., and LeMone, M. A.: Structure and Evolution of the 22 February 1993 TOGA COARE Squall Line: Organization Mechanisms Inferred from Numerical Simulation, *Journal of the Atmospheric Sciences*, 54, 386 – 407, [https://doi.org/10.1175/1520-0469\(1997\)054<0386:SAEOTF>2.0.CO;2](https://doi.org/10.1175/1520-0469(1997)054<0386:SAEOTF>2.0.CO;2), 1997.
- Weyn, J. A. and Durran, D. R.: The Dependence of the Predictability of Mesoscale Convective Systems on the Horizontal Scale and Amplitude of Initial Errors in Idealized Simulations, *Journal of the Atmospheric Sciences*, 74, 2191 – 2210, <https://doi.org/https://doi.org/10.1175/JAS-D-17-0006.1>, 2017.
- 1095 Wilhelm, J., Mohr, S., Punge, H. J., Mühr, B., Schmidberger, M., Daniell, J. E., Bedka, K. M., and Kunz, M.: Severe thunderstorms with large hail across Germany in June 2019, *Weather*, 76, 228–237, <https://doi.org/https://doi.org/10.1002/wea.3886>, 2021.
- Zängl, G., Reinert, D., Rípodas, P., and Baldauf, M.: The ICON (ICOsahedral Non-hydrostatic) modelling framework of DWD and MPI-M: Description of the non-hydrostatic dynamical core, *Quarterly Journal of the Royal Meteorological Society*, 141, 563–579, 2015.
- Zhang, F.: Dynamics and structure of mesoscale error covariance of a winter cyclone estimated through short-range ensemble forecasts, AMETSOC, <https://doi.org/10.1175/MWR3009.1>, 2005.
- 1100 Zhang, F., Bei, N., Rotunno, R., Snyder, C., and Epifanio, C. C.: Mesoscale Predictability of Moist Baroclinic Waves: Convection-Permitting Experiments and Multistage Error Growth Dynamics, *Journal of the Atmospheric Sciences*, 64, 3579–3594, <https://doi.org/10.1175/jas4028.1>, 2007.
- Zhang, F., Sun, Y., Magnusson, L., Buizza, R., Lin, S., Chen, J., and Emanuel, K.: What Is the Predictability Limit of Midlatitude Weather?, 1105 *Journal of the Atmospheric Sciences*, 76, 1077 – 1091, <https://doi.org/10.1175/JAS-D-18-0269.1>, 2019.